This is the preprint of the contribution published as:

Xia, S., Chen, F., Shi, Z., Deng, L., **Georgi, A.**, **Zhang, H.** (2024):
In situ grown single-atom cobalt on carbon nanofibers for efficient adsorptive removal of antibiotics: Performance and mechanisms understanding
Chem. Eng. J. **499** , art. 156594

The publisher's version is available at:

https://doi.org/10.1016/j.cej.2024.156594

In situ grown single-atom cobalt on carbon nanofibers for efficient adsorptive removal of antibiotics: performance and mechanisms understanding

Simeng Xia[a,b], Fan Chen[a,b], Zhou Shi[a,b], Lin Deng[a,b,*], Anett Georgi[c], Haojie Zhang[c,*]

a. Hunan Engineering Research Center of Water Security Technology and Application, College of Civil Engineering, Hunan University, Changsha 410082, China

b. Key Laboratory of Building Safety and Energy Efficiency, Ministry of Education, College of Civil Engineering, Hunan University, Changsha 410082, China

c. Helmholtz Centre for Environmental Research-UFZ, Department of Technical Biogeochemistry, Leipzig 04318, Germany

*Corresponding authors

E-mail addresses: lindeng@hnu.edu.cn (L. Deng); haojie.zhang@ufz.de (H. Zhang)

Abstract

Single-atom cobalt on carbon materials have emerged as a highly promising candidate in catalysis, whereas their contribution to the adsorption of organic pollutants is rarely reported; especially adsorption mechanisms between cobalt and organics remain obscure. In this work, single-atom cobalt incorporated carbon nanofibers (Co_{SA}-CNF) was synthesized via the electrostatic spinning technique. Co_{SA}-CNF showed efficient adsorption for both sulfadiazine (SDZ) and roxarsone (ROX), with q_e values of 413.16 and 338.42 mg/g fitted by the Langmuir-Freundlich isotherm at room temperature. Characterizations and density functional theory (DFT) calculations illustrated that Co_{SA}-CNF carrying two configurations ($Co{-}N_3$ and $Co{-}N_4$) preferred to adsorb SDZ and ROX at $Co{-}N_3$ sites with higher adsorption energy. The continuous-flow tests in a filtration cell with a Co_{SA}-CNF membrane showed the membrane exhibited a superior recyclability and robust durability for SDZ and ROX removal during 54 h continuous operation without obvious decline. Moreover, the membrane was able to be rapidly regenerated by peroxymonosulfate (PMS) activation. In all, this study reports single-atom cobalt incorporated CNF as an efficient adsorbent for eliminating organic pollutants with the advantage of rapid regeneration, and demonstrates that the $Co{-}N_3$ configuration is more favorable to adsorb organics than the $Co{-}N_4$ configuration.

Keywords: Single-atom cobalt; Carbon nanofibers; Sulfadiazine and roxarsone; Adsorption mechanisms; DFT calculations

1. Introduction

Roxarsone (ROX) is the most economical organic arsine that has been used in poultry feeds for disease prevention, growth promotion, feed utilization and meat pigmentation improvement. Sulfadiazine (SDZ) is a highly soluble and chemically stable antibiotic. Due to its broad antimicrobial spectrum and low price, SDZ is diffusely used in conjunction with ROX in aquaculture industries [1, 2]. As a result, their residuals released into surface water and groundwater resources raises public concerns about aquatic pollution. The long-term enrichment of antibiotics in humans may lead to allergic reactions, bacterial resistance as well as teratogenic, mutagenic, and carcinogenic effects [3]. More seriously, when exposed to the environment, ROX can be gradually converted to inorganic arsenic, which is more mobile and toxic. Thus, finding facile and effective strategies for minimizing SDZ and ROX concentrations in residual effluents and water bodies is highly demanded to avoid the potential ecotoxicity and health threats.

Several approaches including advanced oxidation processes (AOPs) [4, 5], biological treatment [6, 7], and adsorption [8, 9] have been put forward for mitigating SDZ and ROX pollution. Among these techniques, adsorption is considered as the simplest and most effective one, which does not produce toxic by-products and secondary pollutants in the process of removing pollutants and shows great potential in practical application [10]. Up to now, a variety of adsorbents such as clay [11], carbon nanotubes [12], activated carbon [13], biochar [14], metal oxides [15], metal organic frameworks (MOFs) [3] and MOF-based composites [16] have been reported

for the adsorption of organic pollutants. Unfortunately, most of these adsorbents suffer from certain drawbacks, including narrow pH adaption, poor adsorption capacity, unsatisfactory recyclability, and difficult separation properties. To overcome these shortcomings, it is of significant importance to design ideal adsorbents with fast removal kinetics, high adsorption affinity, excellent recyclability and environmental friendliness.

Single-atom metals with metal atoms atomically dispersed, have emerged as a highly promising candidates in catalysis, electrocatalysis, and photocatalysis owing to the coordinative unsaturation of metal atoms, excellent catalytic activity, and structural stability [17, 18]. Nevertheless, because of the high surface energy, single atom metals tend to aggregate easily, thereby losing their catalytic activity in synthesis and catalytic reaction processes [19, 20]. To prevent the aggregation and alter the local electronic structure and coordination environment, porous materials of graphene, MOFs, and polymers that can provide numerous anchoring sites and guarantee high dispersion and stability have been used as supports [21, 22]. For example, Chen et al. [23] synthesized single atom copper sites embedded in rGO to activate peroxymonosulfate (PMS) for sulfamethoxazole degradation. Qian et al. [24] reported that FeN_4 structures on carbon nanotubes showed impressive and selective reactivity over a wide pH range of 3.0−9.0 in PMS activation for organic pollutants degradation. Although great achievements have been made in the use of single-atom metals in heterogeneous catalysis, very limited effort has been devoted to examining the adsorption behavior and mechanisms of single-atom metal-based nanomaterials

for organic pollutants.

Zeolitic imidazolate frameworks (ZIFs) consisting of carbon and nitrogen species coordinated with transition metals are known for their fascinating stability and high tolerance for high temperature and harsh chemical environment, making it a promising precursor for single-atom metal construction [25]. Carbon nanofibers (CNFs) with cylindrical structures can provide enough sites for metal atoms and greatly enhance the dispersion and uniformity of metal atoms via the strong interaction between metal atoms and adjacent carbon atoms [26].

In this study, single-atom cobalt-incorporated carbon nanofibers (Co_{SA}-CNF) were successfully prepared using ZIFs as the template and used as the adsorbent to remove SDZ and ROX from aqueous solutions. The morphology and physicochemical properties of Co_{SA}-CNF were systematically characterized. Adsorption kinetics, isotherms and thermodynamics were studied in details. The underlying adsorption mechanisms of SDZ and ROX onto Co_{SA}-CNF was firstly unveiled theoretically by density functional theory (DFT) calculations. Further, a membrane adsorption device was designed to remove SDZ and ROX in continuous flow mode, and the long-term stability of the continuous flow test verified the huge potential of Co_{SA}-CNF for practical application for organic pollutants removal.

2. Experimental and methods

2.1. Reagents

SDZ, ROX, and 2-methylimidazole (MeIM) were obtained from Shanghai Macklin Biochemical Technology Co., Ltd (Shanghai, China). Dimethylimidazole and

other reagents were obtained from Sinopharm Chemical Reagent Co., Ltd. (Beijing, China). All chemicals were analytical pure and utilized as received without any further purification. All solutions were prepared with ultrapure water produced from an ultrapure water purification system (Veolia Water Solutions & Technologies).

2.2. Synthesis strategy and characterization of Co_{SA}-CNF

At first, $Zn(NO_3)_2 \cdot 6H_2O$ (5.94 g) and $Co(NO_3)_2 \cdot 6H_2O$ (0.29 g) were dissolved in 200 mL ultrapure water and stirred to produce a uniform solution A. Meanwhile, 45 g of MeIM was dissolved in 800 mL ultrapure water to form a uniform solution B. Then, solution B was added into solution A with vigorous stirring for 4 h at room temperature. Upon completion, the precipitate was centrifuged, washed and dried in vacuum at 333 K for 12 h to obtain Co-ZIF. ZIF was synthesized through the same procedure without the addition of $Co(NO_3)_2 \cdot 6H_2O$.

Co_{SA}-CNF was then synthesized through an electrospinning process according to Figure 1a. Initially, 1 g of polyacrylonitrile (PAN) was dissolved in 9.3 g of *N,N*-dimethylformamide (DMF) and stirred overnight to obtain the electrospinning precursor solution. Subsequently, 1 g of ZIF was added to the precursor solution and stirred continuously. The resulting solution was then pumped into a plastic syringe (20 mL) with a flow rate of 1.0 mL/h through a steel needle (1.2×30 mm) connected to a power supply at 21 kV. The electrospun fiber was collected on a drum located 8 cm away from the needle at a relative humidity of 40% and a temperature of 301 K. Thereafter, the resulting electrospun nanofiber slice was subjected to a heat treatment process, in which it was heated at 553 K for 2 h in air and then calcined at 1183 K for

2 h under a N_2 flow to produce Co_{SA}-CNF. For comparison, the pure carbon nanofiber (CNF) was synthesized without adding Co-ZIF, and carbon materials loaded with single cobalt atoms (Co_{SA}-C) were obtained by direct pyrolysis of Co-ZIF. Details of characterization techniques are presented in Text S1.

2.3. Batch adsorption experiments

In a standard adsorption experiment, 5 mg of Co_{SA}-CNF was introduced into 50 mL of a 10 mg/L SDZ and ROX solution. The mixture was placed in a temperature-regulated water bath and subjected to agitation at 298 K for 60 min. At specific time intervals, 0.5 mL of liquid sample was withdrawn and filtered using a 0.22 μm syringe filter (ANPEL Laboratory Technologies (Shanghai) Inc) for the quantification of the SDZ and ROX concentration remaining in the filtrate. Unless specified otherwise, the pH of the solution was maintained at its initial value (pH=5.6) without adjustments. The influence of various parameters on the adsorption process was investigated, including pH levels (4, 6, 8, 10, and 12), adsorbent dosage (2.5, 5, and 10 mg), temperature (298, 308, and 318 K), and the presence of coexisting anions (NO_3^-, Cl^-, SO_4^{2-}, and CO_3^{2-}) as well as cations (Na^+, K^+, Mg^{2+}, and Ca^{2+}). The removal rate and adsorption capacity were computed using equations of $(C_0 - C_t)/C_0$ and $(C_0 - C_t)\times V/m$, respectively; and the adsorption coefficient (K_d) for the adsorption of SDZ and ROX was calculated in accordance with the equation of $(C_0 - C_t)\times V/C_t\times m$, where C_0 (mg/L) and C_t (mg/L) were the initial and final SDZ and ROX concentration, V (mL) was the volume of SDZ and ROX solution, and m (g) was the adsorbent amount. Adsorption kinetics tests were studied at contact times ranging from 1 to 180 min at

298 K. Adsorption isotherms tests were carried out at initial SDZ concentrations of 10−40 mg/L and initial ROX concentrations of 10−60 mg/L. Solution pH values were adjusted using 0.1 M HCl or NaOH if necessary. Preliminary adsorption tests showed that the pH of SDZ solution and ROX solution kept steady when the as-synthesized Co_{SA}-CNF was added. All experiments were performed in three parallels for error analysis. Analytical methods are presented in Text S2. Adsorption kinetics, isotherms, and thermodynamic calculation methods are provided in Text S3−S5.

2.4. Continuous-flow adsorption test operation

In view of practical application, a continuous-flow adsorption test was carried out. A piece of Co_{SA}-CNF membrane synthesized via the electrospinning method was placed on a 0.45 μm extraction membrane (a nylon membrane with pore size of 0.45 μm). It was then put on the bottom of a filtration cell. The feed stream containing SDZ (10 mg/L) and ROX (10 mg/L) was pumped through the cell by a peristaltic pump. At predetermined time intervals, water sample was withdrawn for the residual SDZ and ROX concentration determination. To regenerate the Co_{SA}-CNF membrane, 0.5 mL of PMS (0.1 mM) was injected into the reactor as the single-atom cobalt can activate PMS to decompose the adsorbed SDZ and ROX on the membrane. Thereafter, the regenerated membrane was used for the subsequent adsorption run.

2.5. Theoretical computational details

To further elucidate the adsorption mechanisms of SDZ and ROX onto Co_{SA}-CNF, spin-polarized density functional theory (DFT) calculations were conducted

using the Vienna ab-initio simulation package (VASP) [27, 28]. DFT calculations utilized the Projector augmented wave method [28] with a cutoff energy of 400 eV and the Perdew-Burke-Ernzerhof functional [29]. A Grimme dispersion-corrected density function theory (DFT-D3) was accounted for van der Waals interactions [30]. The surface structure was simulated using a 10×10 supercell with a vacuum layer of 20 Å. With regard to carbon nanofibers, we built the structure with a diameter direction and included a vacuum layer of 20 Å. Both models were fully relaxed, with energy convergence setting at 10^{-5} eV and force convergence setting at 0.02 eV/Å. The adsorption energy (E_{ads}) was determined using Eq. 1.

$$E_{ads} = E_{total} - E_{substrate} - E_{adsorbate} \qquad (1)$$

E_{total}, $E_{substrate}$, and $E_{adsorbate}$ represent the energy of adsorption structure, substrate and adsorbate, respectively. Note that DFT calculations in this work were performed to elucidate the interaction between Co_{SA}-CNF and targeted pollutants, such as SDZ and ROX, to enhance our understanding of their bonding mechanisms.

3. Results and discussion

3.1. Characterization

Figure 1b–d show SEM images of ZIF, CNF and Co_{SA}-CNF. Obviously, ZIF displays a 3D star-like shape, with diameter of ~800 nm (Figure 1b). CNF presents a smooth network-like nano-architecture, produced by interactions of nanofibers, with a diameter of ~150 nm (Figure 1c). Co_{SA}-CNF maintains the tubular structure with an increased diameter to 500–700 nm, along with some star-like particles distributing on the surface. That is, even after performing electrostatic spinning and high-temperature

treatment, the ZIF template can maintain its original morphology and is bound to CNF stably. No dark area was recorded via TEM analysis (Figure 3e), indicating the absence of Co atom aggregation. To more clearly observe the atomic structure of the Co_{SA}-CNF, high-angle annular dark field scanning TEM (HAADF-STEM) was conducted as shown in Figure 3f. Many dispersed bright spots (marked with red circles) with a single atom size are clearly spotted over the entire carbon nanofiber matrix, corresponding to Co single-atoms in the sample. In addition, the energy-dispersive spectroscopy (EDS) mapping image shows a uniform distribution of Co, C, and N elements, further disclosing that Co species exists in the form of single atoms rather than nanoparticles or clusters. On the other hand, the homogeneous distribution of Co atoms suggests the migration of Co atoms from the ZIF structure to the CNF support, without obvious elements agglomeration.

To study the chemical state and coordination structure of Co atoms in Co_{SA}-CNF, X-ray absorption near-edge structure (XANES) and extended X-ray absorption fine structure (EXAFS) spectroscopy at the Co K-edge were recorded subsequently. From the Co K-edge XANES spectra in Figure 2a, the absorption edge position of Co_{SA}-CNF is situated between that of bulk Co and CoO, indicating that the oxidation state of Co species in Co_{SA}-CNF is between 0 and +2. According to the Fourier-transformed (FT) EXAFS spectra in Figure 2b, Co_{SA}-CNF only displays one distinct peak at approximately 1.47 Å, which evidences the presence of a large disordered node around the Co atom. The absence of a metallic Co-Co scattering path (≈2.17 Å) also excludes the existence of Co clusters or nanoparticles in Co_{SA}-CNF. The Morlet

wavelets were used to fit the *k*-space data (Figure 2c). As seen, Co_{SA}-CNF only have one intensity maximum at ≈4.8 $Å^{-1}$ for *K* space, originating from the Co−N coordination such as CoPc. This is distinguished from that of Co-foil (7.6 $Å^{-1}$ for *K* space), CoO (6.8 $Å^{-1}$ for *K* space), and Co_3O_4 (6.4 $Å^{-1}$ for *K* space). The WT intensity maximum corresponding to Co−Co coordination does not appear, indicating that Co atoms are present as mononuclear centers rather than in the form of Co−Co band. The fitted EXAFS spectra (Figure S1) and parameters (Table S1) illustrate that the average coordination number of the nearest-neighbor N atoms surrounding the isolated Co atom in Co_{SA}-CNF is 3.57, with a Co−N bond length of 2.07 Å. It is accepted that Co single-atom in ZIF coordinates with four nitrogen to produce the Co-N_4 configuration [31, 32]. Combined with EXAFS fitting results, we speculate that Co atoms in the template of ZIF can migrate to CNF in the high-temperature carbonization process, forming a three-coordinated structure (Co-N_3), while the unmigrated Co atoms remains tetra-coordinated with nitrogen atoms (Co-N_4).

The crystallinity of ZIF, Co_{SA}-C, CNF, and Co_{SA}-CNF was further identified by powder XRD patterns (Figure 3a). The ZIF sample exhibits main characteristic peaks at 2θ of 7.5°, 10.4°, 12.7°, and 18.1°, related to (011), (002), (112), and (222) planes of ZIF-8, respectively [33]. XRD patterns of CNF clearly reveal the appearance of a weak and broad peak at around 25.5°, which is in accordance with the (002) crystal plane of graphic carbon [34]. Surprisingly, Co_{SA}-CNF only shows the characteristic peak of CNF without ZIF crystal and any impurity phase (metallic cobalt or cobalt oxides), suggesting that there is no Co nanoparticles in the sample.

The XPS survey spectra of Co_{SA}-CNF shows the existence of Co, C, N, and O elements, with relative ratios of 0.19%, 92.72%, 3.32%, and 3.77%, respectively (Figure 3b). Yet, the precise mass loading of Co in Co_{SA}-CNF determined by inductively coupled plasma optical emission spectrometry (ICP−OES) is 1.94%. The great difference indicates that majority of cobalt atoms are positioned inside the sample rather than on its surface. Similar to the EDS element mapping image, zinc element was not witnessed as well, resulting from the sublimation of Zn because of the high-temperature pyrolysis (1183 K). The high-resolution Co 2p spectra in Figure 3c is deconvoluted into two individual peaks at 780.2 and 795.9 eV, corresponding to the Co $2p_{1/2}$ and Co $2p_{3/2}$ levels, respectively [35, 36]. This confirms the divalent state of cobalt in the sample [37]. The binding energies at 398.4, 399.8, and 401.2 eV of N 1s spectra (Figure 3d) are separately associated with Co−N, pyrrolic−N, and pyridinic−N [38], with relative contents of 29.6%, 31.0%, and 40.4%, respectively. The appearance of Co−N also validates the formation of Co−N coordination in Co_{SA}-CNF.

To recognize functional groups on the surface of as-synthesized samples, the FTIR spectroscopy of CNF, ZIF, Co_{SA}-C, and Co_{SA}-CNF were recorded as illustrated in Figure 3e. Unlike the pure ZIF, only two characteristic peaks at 3440 and 1606 cm^{-1} retains in Co_{SA}-CNF because of the high-temperature treatment. The two peaks can be ascribed to the O−H stretching mode and C=O vibration [39], respectively. Co_{SA}-CNF possesses the same characteristic peaks as CNF, along with an additional stretching vibration located at 1218 cm^{-1} (C−C bond), suggesting that Co_{SA}-CNF has

a high degree of carbonization. Raman spectra of Co_{SA}-CNF, Co_{SA}-C, and CNF are also performed (Figure 3f). All samples show two characteristic peaks at 1305 and 1582 cm^{-1}, which are related to the D and G bands, respectively. The peak intensities ratio (I_D/I_G) reflects the degree of defect and disorder in the graphite carbons [40]. The I_D/I_G value of Co_{SA}-CNF (0.97) is lower than that of CNF (1.10), indicating more number of defects, improved graphitization degree and greater crystal irregularity. The occurrence of more defective sites in Co_{SA}-CNF can be ascribed to the high-temperature pyrolysis and etching of metal nanoparticles from the support. Especially, the sublimation of zinc can create defects on the carbon plane as well, facilitating the mass transfer in the adsorption process [31].

The Brunauer-Emmett-Teller (BET) surface areas (S_{BET}) of CNF, Co_{SA}-C, ZIF, and Co_{SA}-CNF were obtained by N_2 adsorption/desorption isotherms (Figure S2 and Table S2). Co_{SA}-CNF shows a typical IV-type isotherm accompanied with a H_3 hysteresis loop at relative pressure between 0.6 to 1.0, indicating a mesoporous structure. According to Table S2, the specific surface areas of CNF, Co_{SA}-C, ZIF, and Co_{SA}-CNF are calculated to be 348, 960, 804, and 709 m^2/g, respectively, with mesopore volume values ($V_{mesopore}$) of 0.06, 0.32, 0.06, and 0.54 cm^3/g, respectively. Specifically, the external surface areas ($S_{external}$) of CNF, Co_{SA}-C, ZIF, and Co_{SA}-CNF are 36, 258, 74, and 157 m^2/g, respectively. In contrast with CNF, the low mass incorporation of Co_{SA}-C greatly improves the specific surface area and pore volume of CNF, which endow the Co_{SA}-CNF with more adsorption sites and improved mass transfer ability. In addition, contact angle tests were conducted to examine the

hydrophilicity of Co_{SA}-CNF. As shown in Figure S3, the contact angles of CNF, Co_{SA}-C, ZIF, and Co_{SA}-CNF are 78.11°, 12.98°, 99.43° and 16.60°, indicating Co_{SA}-CNF as a hydrophilic adsorbent. The hydrophilic of Co_{SA}-CNF facilitates the direct permeation of water through the membrane structure by gravity without external pressurization.

Subsequent to the comprehensive characterization analysis proved above, we have successfully synthesized a hydrophilic single-atom cobalt incorporated CNF material, which features high specific surface area and abundant mesopore structure.

3.2. Adsorption capacity evaluation of Co_{SA}-CNF

Initially, the adsorption of SDZ and ROX using CNF, ZIF, Co_{SA}-C, and Co_{SA}-CNF from aqueous solutions was compared as shown in Figure 4a and b. The adsorption ability of CNF could be ignored. And Co_{SA}-C also exhibited very limited removal for SDZ and ROX even though it possessed the highest specific surface area (960 m^2/g) (Table S2). The removal efficiencies of SDZ and ROX by the pristine ZIF reached 19.2% and 31.7%, respectively. In comparison, Co_{SA}-CNF displayed a satisfactory adsorption, with 98.0% and 89.1% removal for SDZ and ROX, respectively. Furthermore, compared with ZIF, the removal of SDZ and ROX adsorbed by ZIF-CNF decreased from 80.1% to 90.2% and 68.3% to 82.0%, while compared with CoSA-C, the adsorption of SDZ and ROX by CoSA-CNF decreased from 80.1% to 90.2% and 68.3% to 82.0%. The removal rates increased from 65.0% to 98.0% and 30.0% to 89.1%, indicating that the increase in the adsorption performance of the composites prepared using electrostatic spinning originated from

the effect of Co atoms on CNF. On the other hand, as shown in Figure S4a and b, Co_{SA}-CNF showed the largest K_d value (5.68 L/Kg and 4.91 L/Kg for SDZ and ROX), definitely indicating that the incorporation of Co single-atoms greatly improved the adsorption capacity. Further, the Co ion leaching from different adsorbents was detected as illustrated in Figure S5. Notably, the Co ion leakage from Co_{SA}-CNF was as low as 0.012 mg/L, which was remarkably lower than that from ZIF (1.79 mg/L) and Co_{SA}-C (1.45 mg/L). The result indicated that Co_{SA}-CNF not only showed excellent adsorption capacity for SDZ and ROX, but also possessed impressive physicochemical structural stability, thereby effectively minimizing the risk of secondary pollution.

Figure S6a and b illustrates the effect of adsorbent concentration on SDZ and ROX. When the dosage of Co_{SA}-CNF was set as 0.05 g/L, the removal rate of SDZ was unsatisfactory due to the limited adsorption sites on the insufficient adsorbent. A complete removal was achieved by increasing the adsorbent concentration to 0.1 g/L. Further improving to 0.2 g/L hardly influenced the removal. The lg (K_d/(L/kg)) value for SDZ adsorption increased from 3.92 to 5.88 (Figure S6c), and the corresponding lg (K_d/(L/kg)) value for ROX enhanced from 3.63 to 5.93 (Figure S6d). pH is also a crucial factor affecting the adsorption process due to its influence on the adsorbent surface charge and targeted pollutants speciation. In this study, the effect of initial pH was studied in pH range of 4−12 as shown in Figure 4c and d. Along with the initial pH increased from 4 to 12, the SDZ removal dropped slightly, with the corresponding lg (K_d/(L/kg)) value decreased from 5.74 to 5.10 (Figure S7a). Similar trend could be

observed in the adsorption of ROX. This was possibly related to the electrostatic repulsive force between the negatively charged Co_{SA}-CNF (Figure S8) and the anionic SDZ and ROX. But, on the whole, the adsorption was not significantly affected by the pH variation. The targeted pollutants removal exceeded 90% even when the pH increased up to 12, suggesting the excellent adaptability of Co_{SA}-CNF to a very wide pH range. In addition, to probe the applicability of Co_{SA}-CNF toward different organic pollutants, carbamazepine (CBZ), sulfamethoxazole (SMX), coumarin (CM), acetaminophen (APAP), and benzoic acid (BA) were also studied as depicted in Figure S9a. Co_{SA}-CNF obtained more than 80% removal for all the organic compounds, with lg (K_d/(L/kg)) values higher than 4.0 (Figure S9b). This clearly implied the high adsorption affinity of Co_{SA}-CNF for different organics with different molecular structures.

In natural water, organic pollutants usually co-exist with various anions (e.g., Cl^-, NO_3^-, CO_3^{2-}, and SO_4^{2-}) and cations (e.g., Na^+, K^+, Mg^{2+} and Ca^{2+}), which may enhance or weaken the removal of SDZ and ROX via competitive adsorption. As shown in Figures S10 and S11, the coexisting Cl^-, NO_3^-, and SO_4^{2-} had almost no influence on the adsorption, even when the concentration increased five times higher than that of the targeted pollutant. However, the presence of CO_3^{2-} (50 mg/L) lowered the removal of SDZ and ROX to 76.7% and 38.9%, respectively (Figure S10d and S11d). This phenomenon was attributed to the functional group (−OH) in carbonate could act as an H acceptor and potentially interact with the O−containing groups on the surface of Co_{SA}-CNF through hydrogen bonding, which was detrimental to the

adsorption [43, 44]. Figures S12 and S13 indicate that the adsorption was barely affected in the presence of Na^+, K^+, Mg^{2+} and Ca^{2+}. Humic acid(HA) was used to investigate the anti-interference ability of Co_{SA}-CNF and the results were shown in Figures S12(e) and S13(e), the negligible impact of HA concentration can be observed on SDZ and ROX removal, even HA concentration up to 50 mg/L. Overall, the excellent anti-interference capability against various anions, cations and HA suggested the remarkable applicability of Co_{SA}-CNF in real water matrix conditions.

3.3. Adsorption kinetics

To better understand the adsorption process, the adsorption kinetics of SDZ and ROX onto Co_{SA}-CNF was studied using pseudo-first-order and pseudo-second-order kinetic models [45]. As shown in Figure 5, ultra-fast adsorption occurred in the first 30 min and then gradually reached equilibrium in the following stage. Based on the fitting curves and correlation coefficients (R^2) in Table S4, the pseudo-second-order model was more appropriate for describing the adsorption kinetic than pseudo-first-order model. Pseudo-first-order kinetic rate constants (k_1) of SDZ adsorption were 1.40, 0.73, and 0.11 min^{-1} at initial SDZ concentrations of 3, 10, and 30 mg/L, respectively. These values were much higher than that of ROX adsorption (0.14, 0.12, and 0.033 min^{-1}), revealing a higher adsorption affinity of Co_{SA}-CNF toward SDZ than ROX [46].

3.4. Adsorption isotherms and thermodynamics

To evaluate the adsorption capacity of Co_{SA}-CNF and to gain experimental

insights into the interaction between targeted pollutants and Co_{SA}-CNF, adsorption isotherms analysis was conducted. Figure 6 illustrates the adsorption of SDZ and ROX onto Co_{SA}-CNF at temperatures of 298, 308, and 318 K. With the increase in equilibrium concentration (C_e) of targeted pollutants, the equilibrium adsorption capacity (q_e) gradually increased, eventually reaching its maximum. Higher temperature seemed to be favorable for the adsorption. Isotherm models of Langmuir, Freundlich, and Langmuir-Freundlich in Text S4 were applied to fit the isotherm data. On the basis of higher R^2 values (Table S5), the isotherms of SDZ and ROX onto Co_{SA}-CNF were all better fitted by the Langmuir-Freundlich model, suggesting the existence of multiple interactions between the heterogeneous surface of the adsorbent and adsorbate [47]. Of note, the R^2 values fitted by Langmuir model was high as well, implying that the adsorption was mono-layer accompanied. And the corresponding theoretical maximum adsorption capacities of SDZ onto Co_{SA}-CNF were 413.16, 436.95, and 465.88 mg/g at 298, 308, and 318 K, respectively. Likewise, the adsorption capacities of ROX were determined as 338.42, 368.43 and 380.74 mg/g, respectively. The remarkable adsorption ability of Co_{SA}-CNF can be emphasized when comparing with other reported adsorbents as summarized in Tables S6 and S7. Generally speaking, observation of elevated K_F or K_L values, correlating to the binding energy, implies an enhanced propensity for the adsorption process. According to Table S5, K_F and K_L values in the case of SDZ adsorption onto Co_{SA}-CNF were higher than those of ROX adsorption, indicating a higher adsorption capacity of Co_{SA}-CNF for SDZ than ROX.

To provide an intrinsic understanding about the internal energy change during the adsorption, thermodynamic calculations were conducted using methods described in Text S5. Thermodynamic parameters including standard Gibbs energy change (ΔG^0, kJ/mol), standard enthalpy change (ΔH^0, kJ/mol) and standard entropy change (ΔS^0, J/(mol·K)) were calculated according to the van't Hoff equation. As listed in Table S8, for the adsorption of SDZ at temperatures of 298, 308, and 318 K, the ΔG^0 values were determined as −18.36, −19.43, and −20.13 kJ/mol, respectively, while the adsorption of ROX as −10.40, −10.75, and −11.60 kJ/mol, respectively. The negative ΔG^0 and positive ΔH^0 values revealed that the adsorption of SDZ and ROX onto Co_{SA}-CNF was endothermic and more favorable at higher temperatures. The positive value of ΔS^0 (88.79 J/mol·K for SDZ and 59.36 J/mol·K for ROX) implied an increased disorder of the solid-solution system.

In addition, to prove the physicochemical structure stability, Co_{SA}-CNF after adsorption of SDZ and ROX (denoted as Co_{SA}-CNF-SDZ and Co_{SA}-CNF-ROX) was further characterized by XRD patterns, FTIR spectroscopy, and Raman spectra (Figure S12). Figure S14a clearly shows that both Co_{SA}-CNF-SDZ and Co_{SA}-CNF-ROX possessed characteristic peaks as the fresh one, evidencing the structural stability of Co_{SA}-CNF. Also, as shown in Figure S14b, the characteristic absorption peaks of the exhausted Co_{SA}-CNF remained the same like the fresh one. The slight decrease in I_D/I_G value in the used adsorbent indicated the improved degree of defect and disorder in the graphite carbon resulted from the adsorption of SDZ and ROX (Figure S14c). Further, Figure S15 compares N_2 adsorption-desorption isotherms and

pore size distributions of Co_{SA}-CNF-SDZ and Co_{SA}-CNF-ROX. In contrast with Co_{SA}-CNF (709 m^2/g), the specific surface area of Co_{SA}-CNF-SDZ and Co_{SA}-CNF-ROX sharply declined to 82 and 163 m^2/g (Table S9), respectively, due to the occupation of pollutants onto/into the adsorbent.

3.5. Adsorption mechanisms investigation

In adsorption tests, both CNF and ZIF achieved very limited adsorption of SDZ and ROX, while single-atom cobalt incorporated CNF achieved high adsorption capacity. To gain a better understanding of interactions between Co atoms and targeted pollutants, the involved adsorption mechanisms were analyzed using XPS analysis. Figure 7a depicts the high-resolution C 1s spectrum. Compared to the fresh Co_{SA}-CNF, the peaks associated with C−O (285.9 eV), C=O (289.1 eV), and O−C=O (291.7 eV) shifts to lower binding energies of 285.4, 288.3, and 290.8 eV in Co_{SA}-CNF-SDZ and 285.8, 288.9, and 290.3 eV in Co_{SA}-CNF-ROX, respectively, indicating the possibility of electron redistribution through π−π EDA interactions [48]. The high-resolution O 1s spectrum shows three individual peaks at 532.9, 531.9, and 530.7 eV (Figure 7b), which are in accordance with C=O, R−OH, and Co−O bonds [49], respectively. After the adsorption, the relative content of R−OH declines to 37.0% and 33.7%, suggesting the participation of hydrogen bonding interactions between Co_{SA}-CNF and SDZ (ROX). Meanwhile, the relative content of Co−O bond increases from 7.4% to 14.7% and 32.5%, demonstrating the bond of single-atom cobalt in Co_{SA}-CNF with the O atom in SDZ and ROX. In the high-resolution N 1s spectrum (Figure 7c), three component peaks at 401.2, 399.8, and 398.4 eV

corresponds to quaternary−N, pyrrolic−N, and Co−N bonds, respectively. The increased Co−N content highlights the interaction between Co atoms in Co_{SA}-CNF and N atoms in SDZ and ROX.

Further, to uncover adsorption mechanisms of SDZ and ROX (Figure S16) onto Co_{SA}-CNF at the atomic level, DFT calculations were optimized to calculate the surface geometries and atomic adsorption configurations. The optimized adsorption configurations of SDZ and ROX onto Co_{SA}-CNF at Co−N_4 and Co−N_3 sites and corresponding adsorption energies (E_{ads}) are presented in Figure 8. The interaction energies of adsorbed SDZ molecules on Co_{SA}-CNF at Co−N_4 site were −0.66, −0.60, and −0.50 eV with three optimized binding forms, and the corresponding Co−N bond lengths were 2.36, 2.29, and 3.58 Å, respectively. With regard to the Co−N_3 site, the corresponding E_{ads} values were calculated as −1.28, −0.87, and −1.81 eV, along with the Co−N bond length being 2.08, 2.03, and 2.04 Å, respectively. Note that the adsorption energy of SDZ at Co−N_3 site was much higher than that at Co−N_4 site. Similar trend was spotted in ROX adsorption. With three optimized binding forms, the E_{ads} values of ROX at Co−N_4 site were −0.40, −0.88, and −1.03 eV, which were much larger than that at Co−N_3 site (−1.14, −1.33, and −2.37 eV). The DFT calculations result demonstrated that Co−N_3 site was more favorable to the adsorption of organic pollutants than Co−N_4 site. Moreover, according to the differential charge and Bader calculations results in Figure S17, during the adsorption process of SDZ by Co_{SA}-CNF, 0.064 electrons shifted from SDZ to the Co-N_4 site, accompanied by 0.043 electrons transferring from the Co-N_3 site to SDZ. As for the adsorption of ROX,

0.067 electrons migrated from ROX to the Co-N_4 site, along with 0.94 electrons shifting from the Co-N_3 site to ROX (Figure S18). Notably, compared to the Co-N_4 site, the Co-N_3 cite tended to provide much more electrons to both SDZ and ROX, resulting in a stronger adsorption energy.

On the basis of the above analysis, the enlarged external specific surface area and mesopore volume, π-π EDA interactions, and the formation of Co−N and Co−O bonds between Co and targeted pollutants all contributed to the high adsorption capacity of Co_{SA}-CNF. More specifically, single-atom cobalt in the form of Co−N_3 was more favorable to organic pollutants adsorption than in the form of Co−N_4. Accordingly, adsorption mechanisms of SDZ and ROX on Co_{SA}-CNF was proposed as schematically illustrated in Figure 9.

3.6. Recyclability and application

To simulate the practical application of Co_{SA}-CNF in water treatment, a filtration cell for the continuous removal of organic pollutants was designed. The schematic diagram and photograph of the continuous flow filtration cell is schematically depicted in Figure 10a. Batch adsorption tests were carried out to treat 500 mL of antibiotic wastewater containing SDZ (10 mg/L) and ROX (10 mg/L). As shown in Figure 10b, over 99% of SDZ and ROX could be removed in 9 h in the first run. As cobalt can be used to activate PMS to degrade pollutants, 0.5 mL of PMS (0.1 mM) was added to achieve the regeneration of Co_{SA}-CNF membrane in this study. The adsorption performance of Co_{SA}-CNF membrane was almost fully maintained when undergoing the subsequent run. After six consecutive runs, the removal maintained

~98%, indicating superior recyclability and robust durability of Co_{SA}-CNF. The result indicated that the Co_{SA}-CNF membrane possessed excellent regeneration performance and had good application potential in small-scale adsorption system to treat organics contaminated water in continuous flow mode.

4. Conclusions

Co_{SA}-CNF was synthesized via the electrostatic spinning technique by immobilizing the template of zeolitic imidazolate framework on carbon nanofibers for the adsorption of organic pollutants. To the best of our knowledge, this study is among the first to report single-atom cobalt incorporated carbon nanofibers with high adsorption capacities for SDZ (413.16 mg/g) and ROX (338.42 mg/g). The adsorption of pollutants onto the materials involves multiple interactions, including cobalt-pollutant interaction, hydrophobic interaction, and π-π interaction. Characterizations and density functional theory (DFT) calculations illustrate that the single-atom cobalt in Co_{SA}-CNF exists in two configurations, *i.e.*, $Co{-}N_3$ and $Co{-}N_4$. Both SDZ and ROX prefer to be adsorbed at $Co{-}N_3$ sites, with the highest adsorption energies of −1.81 and −2.37 eV, respectively, accompanied by −0.66 and −1.03 eV at $Co{-}N_4$ sites. The performance of the Co_{SA}-CNF membrane filtration cell showed no obvious decline for the elimination of SDZ and ROX contaminated water during 54 h continuous flow adsorption test with regeneration by PMS activation, showcasing the huge application potential of Co_{SA}-CNF membrane. In conclusion, this study provides a highly efficient adsorbent of single-atom cobalt incorporated carbon nanofibers, and clarifies that $Co{-}N_3$ configuration is more favorable for adsorbing organic pollutants

than the $Co-N_4$ configuration. The adsorption membranes developed based on Co_{SA}-CNF can be rapidly regenerated, offering valuable insights for the development of adsorbents with potential applications.

Acknowledgments

This work was supported by the National Natural Science Foundation of China (52270004) and The Science and Technology Innovation Program of Hunan Province (2021RC3039). Haojie Zhang acknowledges funding from the Sino-German (CSC-DAAD) Postdoc Scholarship Program (57607866) and the Alexander von Humboldt foundation for postdoctoral fellowship.

References

[1] A.K. Priya, L. Gnanasekaran, S. Rajendran, J. Qin, Y. Vasseghian, Occurrences and removal of pharmaceutical and personal care products from aquatic systems using advanced treatment- A review, Environmental Research, 204 (2022) 112298.

[2] W. Baran, E. Adamek, J. Ziemiańska, A. Sobczak, Effects of the presence of sulfonamides in the environment and their influence on human health, Journal of Hazardous Materials, 196 (2011) 1-15.

[3] L. Han, P. Qin, M. Li, D. Li, M. Mu, Y. Gao, S. Zhu, M. Lu, Z. Cai, Hierarchically porous zirconium-based metal–organic frameworks for rapid adsorption and enrichment of sulfonamide antibiotics, Chemical Engineering Journal, 456 (2023) 140969.

[4] H. Zhang, L. Deng, J. Chen, Y. Zhang, M. Liu, Y. Han, Y. Chen, H. Zeng, Z. Shi, How MoS2 assisted sulfur vacancies featured Cu2S in hollow Cu2S@MoS2 nanoboxes to activate H2O2 for efficient sulfadiazine degradation?, Chemical Engineering Journal, 446 (2022) 137364.

[5] S. Gong, J. Yang, Q. Pan, X. Liu, Q. Zhang, D. Wang, Simultaneous oxidation of roxarsone and adsorption of released arsenic by FeS-activated sulfite, Water Research, 237 (2023) 119979.

[6] L. Zhu, J. Ma, H. Yuan, L. Deng, Z. Shi, Q. He, S. Ke, Effects of successional sulfadiazine exposure on biofilm in moving bed biofilm reactor: Secretion of extracellular polymeric substances, community activity and functional gene expression, Bioresource Technology, 380 (2023) 129092.

[7] X. Wang, Q. Wu, Z.-Z. Wang, W.-J. Ma, J. Qiu, N.-S. Fan, R.-C. Jin, Biotransformation-mediated detoxification of roxarsone in the anammox process: Gene regulation mechanism, Chemical Engineering Journal, 467 (2023) 143449.

[8] Z. Zhang, L. Sun, Z. Pei, H. Li, L. Wang, J. Ma, Y. Li, R. Yang, Q. Zhang, New insight into the adsorption of sulfadiazine on graphite-like biochars prepared at different pyrolytic temperatures, Journal of Cleaner Production, 413 (2023) 137468.

[9] W.-R. Chen, C.-H. Huang, Surface adsorption of organoarsenic roxarsone and ar nilic acid on iron and aluminum oxides, Journal of Hazardous Materials, 227-228 (2012) 378-385.

[10] P. Shao, Z. Chang, M. Li, X. Lu, W. Jiang, K. Zhang, X. Luo, L. Yang, Mixed-valence molybdenum oxide as a recyclable sorbent for silver removal and recovery from wastewater, Nature Communications, 14 (2023) 1365.

[11] G.G. Hacıosmanoğlu, C. Mejías, J. Martín, J.L. Santos, I. Aparicio, E. Alonso, Antibiotic adsorption by natural and modified clay minerals as designer adsorbents for wastewater treatment: A comprehensive review, Journal of Environmental Management, 317 (2022) 115397.

[12] C. Xia, H. Huang, D. Liang, Y. Xie, F. Kong, Q. Yang, J. Fu, Z. Dou, Q. Zhang, Z. Meng, Adsorption of tetracycline hydrochloride on layered double hydroxide loaded carbon nanotubes and site energy distribution analysis, Chemical Engineering Journal, 443 (2022) 136398.

[13] F. Yang, C. Jin, S. Wang, Y. Wang, L. Wei, L. Zheng, H. Gu, S.S. Lam, M. Naushad, C. Li, C. Sonne, Bamboo-based magnetic activated carbon for efficient removal of sulfadiazine: Application and adsorption mechanism, Chemosphere, 323 (2023) 138245.

[14] J. Yan, X. Zuo, S. Yang, R. Chen, T. Cai, D. Ding, Evaluation of potassium ferrate activated biochar for the simultaneous adsorption of copper and sulfadiazine: Competitive versus synergistic, Journal of Hazardous Materials, 424 (2022) 127435.

[15] N. El Messaoudi, A. El Mouden, Y. Fernine, M. El Khomri, A. Bouich, N. Faska, Z. Ciğeroğlu, J.H.P. Américo-Pinheiro, A. Jada, A. Lacherai, Green synthesis of Ag2O nanoparticles using Punica granatum leaf extract for sulfamethoxazole antibiotic adsorption: characterization, experimental study, modeling,

and DFT calculation, Environmental Science and Pollution Research, (2022).
[16] J. Yang, X. Zhang, X. Wang, H. Wang, J. Zhao, Z. Zhou, X. Du, X. Lu, In situ anchor of multi-walled carbon nanotubes into iron-based metal-organic frameworks for enhanced adsorption of polycyclic aromatic hydrocarbons by magnetic solid-phase extraction, Journal of Chromatography A, 1681 (2022) 463459.
[17] Y. Chen, R. Gao, S. Ji, H. Li, K. Tang, P. Jiang, H. Hu, Z. Zhang, H. Hao, Q. Qu, X. Liang, W. Chen, J. Dong, D. Wang, Y. Li, Atomic-Level Modulation of Electronic Density at Cobalt Single-Atom Sites Derived from Metal–Organic Frameworks: Enhanced Oxygen Reduction Performance, Angewandte Chemie International Edition, 60 (2021) 3212-3221.
[18] B.-Q. Li, C.-X. Zhao, S. Chen, J.-N. Liu, X. Chen, L. Song, Q. Zhang, Framework-Porphyrin-Derived Single-Atom Bifunctional Oxygen Electrocatalysts and their Applications in Zn–Air Batteries, Advanced Materials, 31 (2019) 1900592.
[19] H. Yu, W. Wang, Q. Mao, K. Deng, Z. Wang, Y. Xu, X. Li, H. Wang, L. Wang, Pt single atom captured by oxygen vacancy-rich NiCo layered double hydroxides for coupling hydrogen evolution with selective oxidation of glycerol to formate, Applied Catalysis B: Environmental, 330 (2023) 122617.
[20] Z. Chen, J. Song, R. Zhang, R. Li, Q. Hu, P. Wei, S. Xi, X. Zhou, P.T.T. Nguyen, H.M. Duong, P.S. Lee, X. Zhao, M.J. Koh, N. Yan, K.P. Loh, Addressing the quantitative conversion bottleneck in single-atom catalysis, Nature Communications, 13 (2022) 2807.
[21] C. Liu, T. Li, X. Dai, J. Zhao, D. He, G. Li, B. Wang, X. Cui, Catalytic Activity Enhancement on Alcohol Dehydrogenation via Directing Reaction Pathways from Single- to Double-Atom Catalysis, Journal of the American Chemical Society, 144 (2022) 4913-4924.
[22] J. Wang, M. Zheng, X. Zhao, W. Fan, Structure-Performance Descriptors and the Role of the Axial Oxygen Atom on M–N4–C Single-Atom Catalysts for Electrochemical CO2 Reduction, ACS Catalysis, 12 (2022) 5441-5454.
[23] F. Chen, X.-L. Wu, L. Yang, C. Chen, H. Lin, J. Chen, Efficient degradation and mineralization of antibiotics via heterogeneous activation of peroxymonosulfate by using graphene supported single-atom Cu catalyst, Chemical Engineering Journal, 394 (2020) 124904.
[24] K. Qian, H. Chen, W. Li, Z. Ao, Y.-n. Wu, X. Guan, Single-Atom Fe Catalyst Outperforms Its Homogeneous Counterpart for Activating Peroxymonosulfate to Achieve Effective Degradation of Organic Contaminants, Environmental Science & Technology, 55 (2021) 7034-7043.
[25] W. Yang, X. Liu, X. Chen, Y. Cao, S. Cui, L. Jiao, C. Wu, C. Chen, D. Fu, I.D. Gates, Z. Gao, H.-L. Jiang, A Sulfur-Tolerant MOF-Based Single-Atom Fe Catalyst for Efficient Oxidation of NO and Hg0, Advanced Materials, 34 (2022) 2110123.
[26] H. Lyu, P. Li, J. Tang, W. Zou, P. Wang, B. Gao, L. Dong, Single-atom Mn anchored on N-doped graphene oxide for efficient adsorption-photocatalytic degradation of sulfanilamide in water: Electronic interaction and mineralization pathway, Chemical Engineering Journal, 454 (2023) 140120.
[27] G. Kresse, J. Furthmüller, Efficient iterative schemes for ab initio total-energy calculations using a plane-wave basis set, Physical Review B, 54 (1996) 11169-11186.
[28] G. Kresse, D. Joubert, From ultrasoft pseudopotentials to the projector augmented-wave method, Physical Review B, 59 (1999) 1758-1775.
[29] J.P. Perdew, K. Burke, M. Ernzerhof, Generalized Gradient Approximation Made Simple, Physical Review Letters, 77 (1996) 3865-3868.
[30] S. Grimme, J. Antony, S. Ehrlich, H. Krieg, A consistent and accurate ab initio parametrization of density functional dispersion correction (DFT-D) for the 94 elements H-Pu, The Journal of Chemical

Physics, 132 (2010).
[31] X. Sun, S. Sun, S. Gu, Z. Liang, J. Zhang, Y. Yang, Z. Deng, P. Wei, J. Peng, Y. Xu, C. Fang, Q. Li, J. Han, Z. Jiang, Y. Huang, High-performance single atom bifunctional oxygen catalysts derived from ZIF-67 superstructures, Nano Energy, 61 (2019) 245-250.
[32] S. Wu, X. Xu, Z. Wang, X. Ke, S. Gu, G. Zhou, L. Wang, Engineering Strategy for Enhancing the Co Loading of Co–N4–C Single-Atomic Catalysts Based on the ZIF-67@Yeast Construction, ACS Applied Materials & Interfaces, 15 (2023) 40451-40458.
[33] D. Saliba, M. Ammar, M. Rammal, M. Al-Ghoul, M. Hmadeh, Crystal Growth of ZIF-8, ZIF-67, and Their Mixed-Metal Derivatives, Journal of the American Chemical Society, 140 (2018) 1812-1823.
[34] Y. Wang, G. Hu, Y. Feng, X. Zhang, C. Song, J. Lin, Y. Huang, Y. Zhang, Z. Liu, C. Tang, C. Yu, Formation of p-BN@Zn/Co-ZIF Hybrid materials for improved photocatalytic CO2 reduction by H2O, Materials Research Bulletin, 152 (2022) 111867.
[35] H. Fei, J. Dong, M.J. Arellano-Jiménez, G. Ye, N. Dong Kim, E.L.G. Samuel, Z. Peng, Z. Zhu, F. Qin, J. Bao, M.J. Yacaman, P.M. Ajayan, D. Chen, J.M. Tour, Atomic cobalt on nitrogen-doped graphene for hydrogen generation, Nature Communications, 6 (2015) 8668.
[36] E.S. Andreiadis, P.-A. Jacques, P.D. Tran, A. Leyris, M. Chavarot-Kerlidou, B. Jousselme, M. Matheron, J. Pécaut, S. Palacin, M. Fontecave, V. Artero, Molecular engineering of a cobalt-based electrocatalytic nanomaterial for H2 evolution under fully aqueous conditions, Nature Chemistry, 5 (2013) 48-53.
[37] K. Shah, R. Dai, M. Mateen, Z. Hassan, Z. Zhuang, C. Liu, M. Israr, W.C. Cheong, B. Hu, R.J.A.C. Tu, Cobalt single atom incorporated in ruthenium oxide sphere: a robust bifunctional electrocatalyst for HER and OER, 134 (2022) e202114951.
[38] J. Wu, H. Zhou, Q. Li, M. Chen, J. Wan, N. Zhang, L. Xiong, S. Li, B.Y. Xia, G.J.A.E.M. Feng, Densely Populated Isolated Single Co□ N Site for Efficient Oxygen Electrocatalysis, 9 (2019) 1900149.
[39] M. Chen, T. Liu, X. Zhang, R. Zhang, S. Tang, Y. Yuan, Z. Xie, Y. Liu, H. Wang, K.V.J.A.F.M. Fedorovich, Photoinduced enhancement of uranium extraction from seawater by MOF/black phosphorus quantum dots heterojunction anchored on cellulose nanofiber aerogel, 31 (2021) 2100106.
[40] S. Xia, L. Deng, X. Liu, L. Yang, X. Yang, Z. Shi, Y. Pei, Fabrication of magnetic nickel incorporated carbon nanofibers for superfast adsorption of sulfadiazine: Performance and mechanisms exploration, Journal of Hazardous Materials, 423 (2022) 127219.
[41] J. Lou, J. An, X. Wang, M. Cheng, Y. Cui, A novel DBD/VUV/PMS process for efficient sulfadiazine degradation in wastewater: Singlet oxygen-dominated nonradical oxidation, Journal of Hazardous Materials, 461 (2024) 132650.
[42] C. Chen, L. Liu, Y. Li, L. Zhou, Y. Lan, Efficient degradation of roxarsone and simultaneous in-situ adsorption of secondary inorganic arsenic by a combination of Co3O4-Y2O3 and peroxymonosulfate, Journal of Hazardous Materials, 407 (2021) 124559.
[43] H. Liu, Y. Wei, J. Luo, T. Li, D. Wang, S. Luo, J.C. Crittenden, 3D hierarchical porous-structured biochar aerogel for rapid and efficient phenicol antibiotics removal from water, Chemical Engineering Journal, 368 (2019) 639-648.
[44] L. Ji, Y. Wan, S. Zheng, D. Zhu, Adsorption of Tetracycline and Sulfamethoxazole on Crop Residue-Derived Ashes: Implication for the Relative Importance of Black Carbon to Soil Sorption, Environmental Science & Technology, 45 (2011) 5580-5586.
[45] G. Tian, W. Wang, L. Zong, Y. Kang, A. Wang, A functionalized hybrid silicate adsorbent derived from naturally abundant low-grade palygorskite clay for highly efficient removal of hazardous

antibiotics, Chemical Engineering Journal, 293 (2016) 376-385.
[46] W. Konicki, K. Cendrowski, X. Chen, E. Mijowska, Application of hollow mesoporous carbon nanospheres as an high effective adsorbent for the fast removal of acid dyes from aqueous solutions, Chemical Engineering Journal, 228 (2013) 824-833.
[47] K. Fu, X. Liu, C. Lv, J. Luo, M. Sun, S. Luo, J.C. Crittenden, Superselective Hg(II) Removal from Water Using a Thiol-Laced MOF-Based Sponge Monolith: Performance and Mechanism, Environmental Science & Technology, 56 (2022) 2677-2688.
[48] Z. Zhang, H. Lan, H. Liu, J. Qu, Removal of tetracycline antibiotics from aqueous solution by amino-Fe (III) functionalized SBA15, Colloids and Surfaces A: Physicochemical and Engineering Aspects, 471 (2015) 133-138.
[49] Y. Yang, G. Zeng, D. Huang, C. Zhang, D. He, C. Zhou, W. Wang, W. Xiong, B. Song, H.J.S. Yi, In situ grown single‐atom cobalt on polymeric carbon nitride with bidentate ligand for efficient photocatalytic degradation of refractory antibiotics, 16 (2020) 2001634.

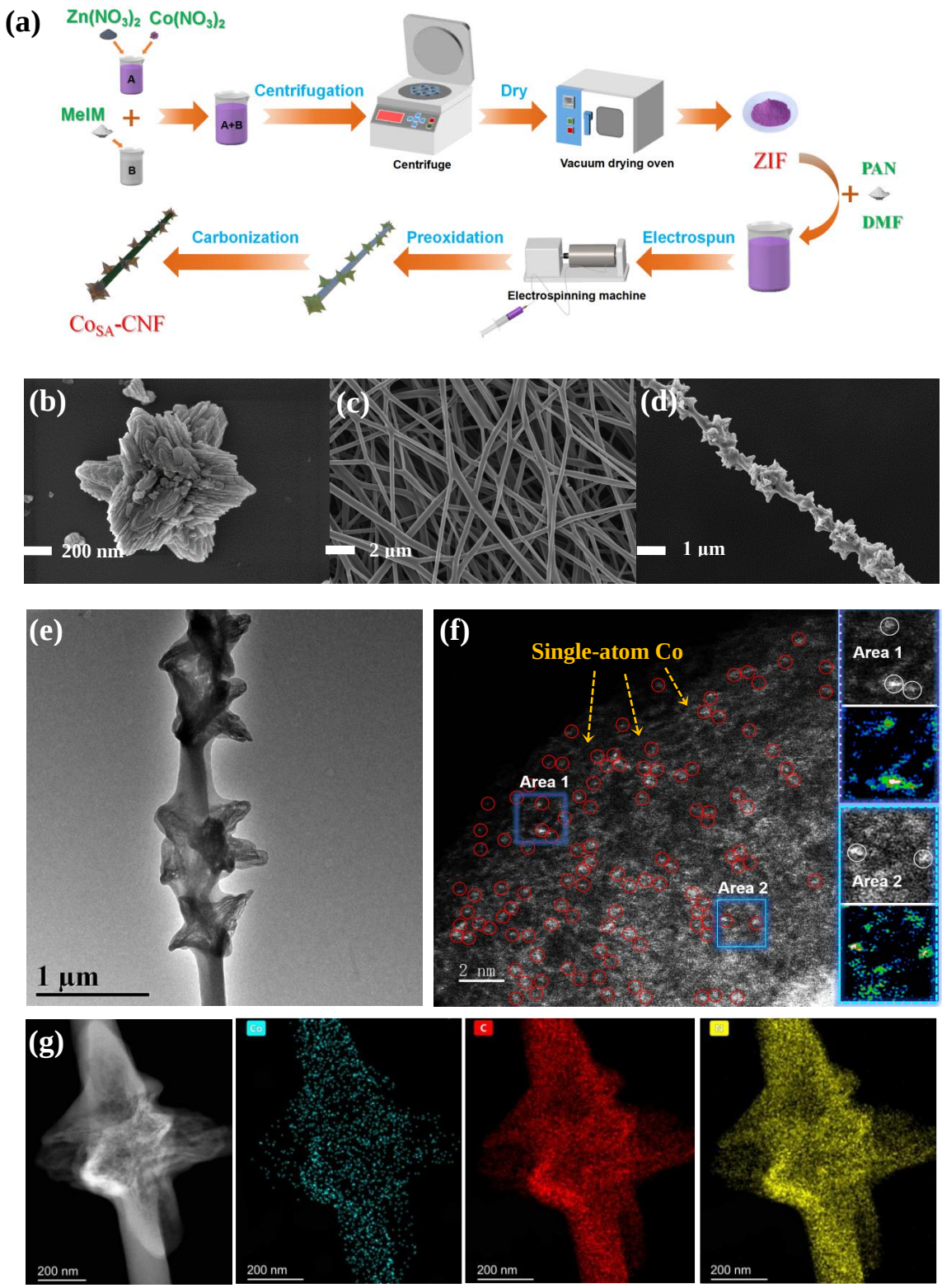

Figure 1. (a) Illustration of the synthesis procedure of Co_{SA}-CNF; SEM images of (b) ZIF, (c) CNF, and (d) Co_{SA}-CNF; (e) TEM image of Co_{SA}-CNF; (f) HAADF-STEM image of Co_{SA}-CNF; (g) EDS mapping image of Co_{SA}-CNF: Co (blue), C (red), N (yellow).

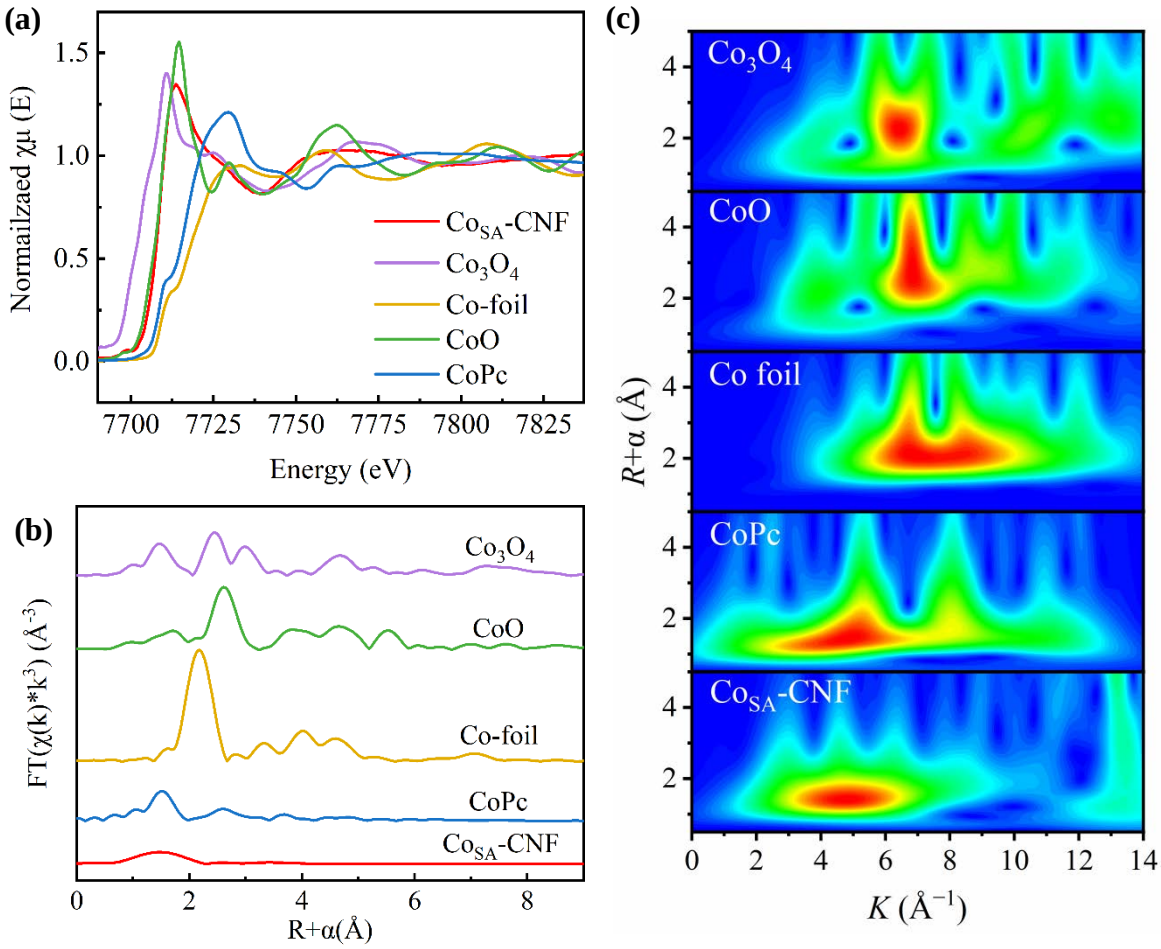

Figure 2. Structural characterization by XAFS spectroscopy: (a) Co K-edge XANES spectra, (b) Fourier-transformed (FT) extended X-ray absorption fine structure (FT-EXAFS) spectra, and (c) wavelet transforms for the EXAFS signals of Co_{SA}-CNF and reference samples.

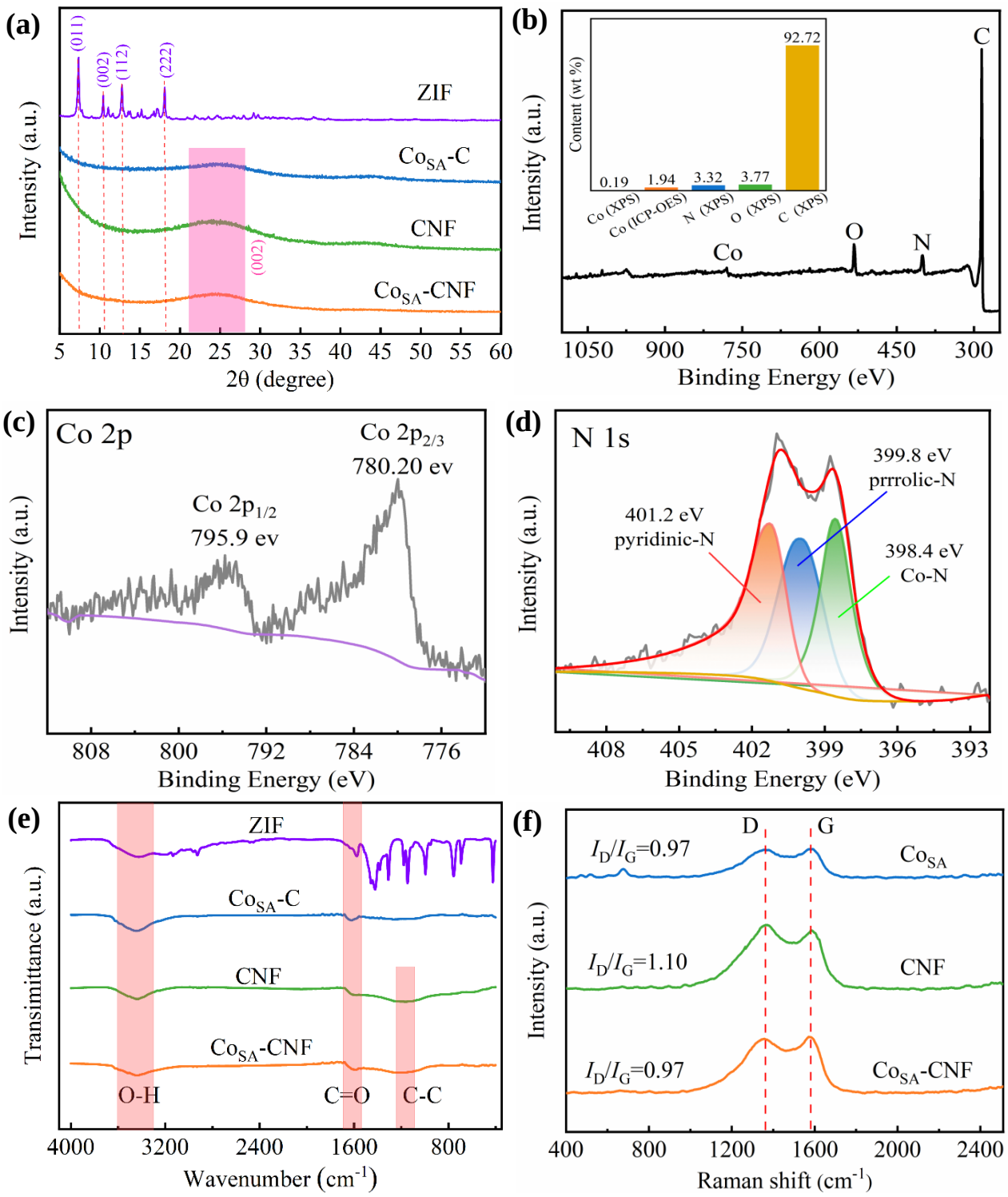

Figure 3. (a) XRD patterns of of ZIF, Co$_{SA}$-C, CNF, and Co$_{SA}$-CNF; (b) XPS survey spectra of Co$_{SA}$-CNF (the inset represents the relative cobalt amount in Co$_{SA}$-CNF) and corresponding XPS narrow spectra of (c) Co 2p and (d) N 1s; (e) FTIR spectrum of ZIF, Co$_{SA}$-C, CNF, and Co$_{SA}$-CNF; (f) Raman spectra of Co$_{SA}$-C, CNF, and Co$_{SA}$-CNF.

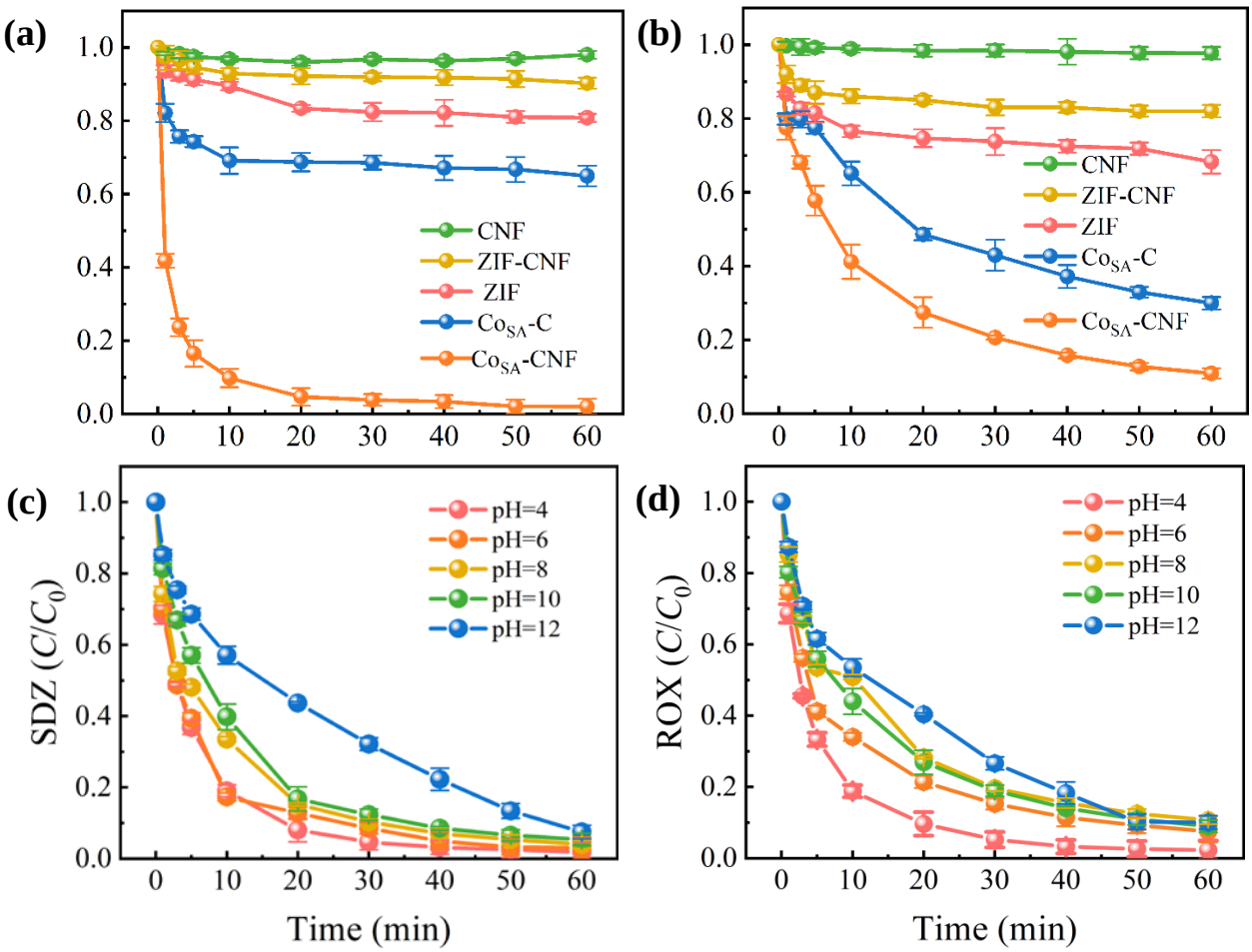

Figure 4. Adsorption of (a) SDZ and (b) ROX by different adsorbents ([SDZ]=[ROX]=10 mg/L, [adsorbent]=0.1 g/L, *T*=298 K); effect of initial pH on (c) SDZ and (d) ROX removal by Co_{SA}-CNF ([SDZ]=[ROX]=10 mg/L, [adsorbent]=0.1 g/L, *T*=298 K).

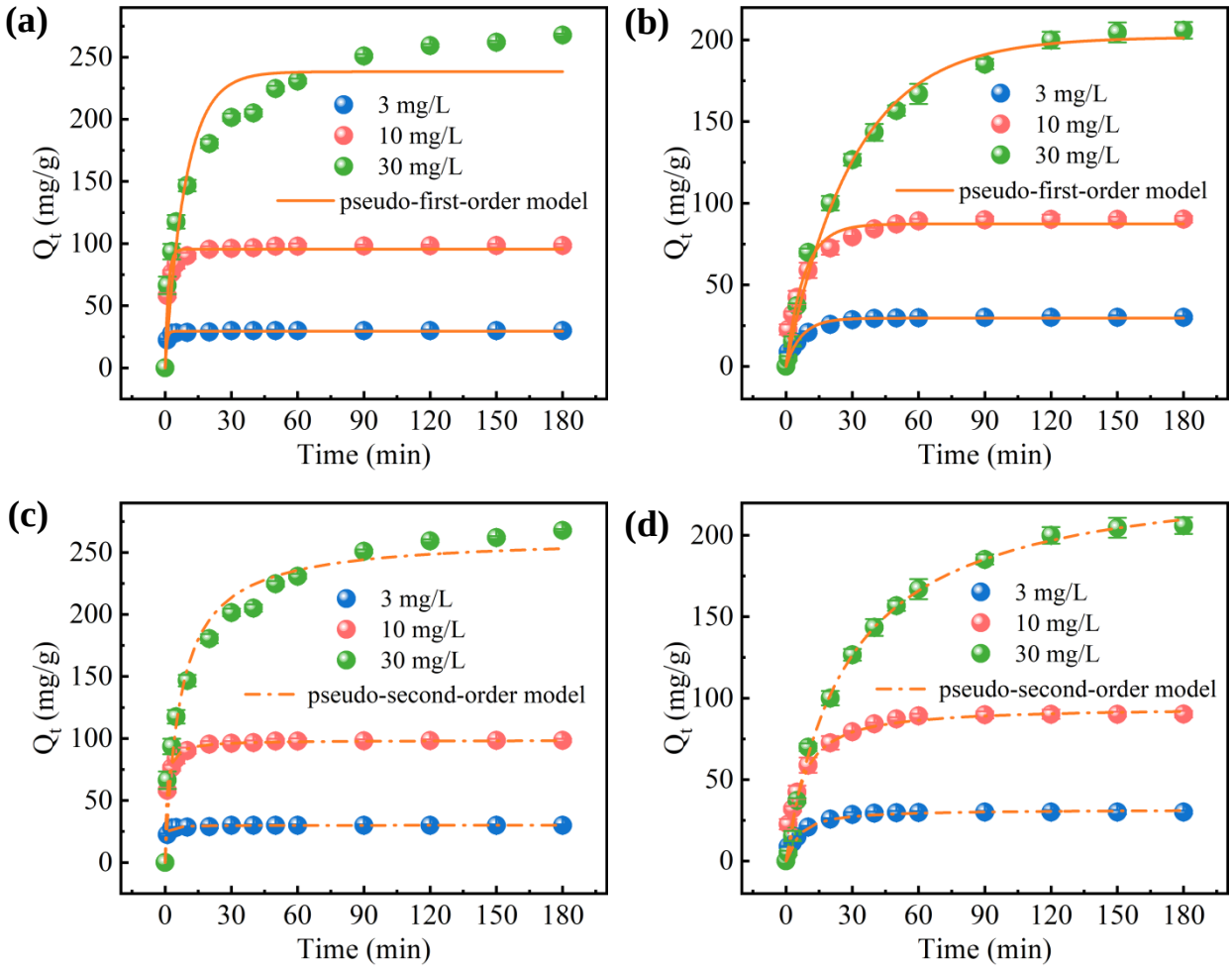

Figure 5. Time-dependent adsorption of SDZ on Co_{SA}-CNF: (a) pseudo-first-order model and (c) pseudo-second-order model ([adsorbent]= 0.1 g/L, pH without pre-adjustment, *T*=298 K); time-dependent adsorption of ROX on Co_{SA}-CNF: (b) pseudo-first-order model and (d) pseudo-second-order model ([adsorbent]=0.1 g/L, pH without pre-adjustment, *T*=298 K).

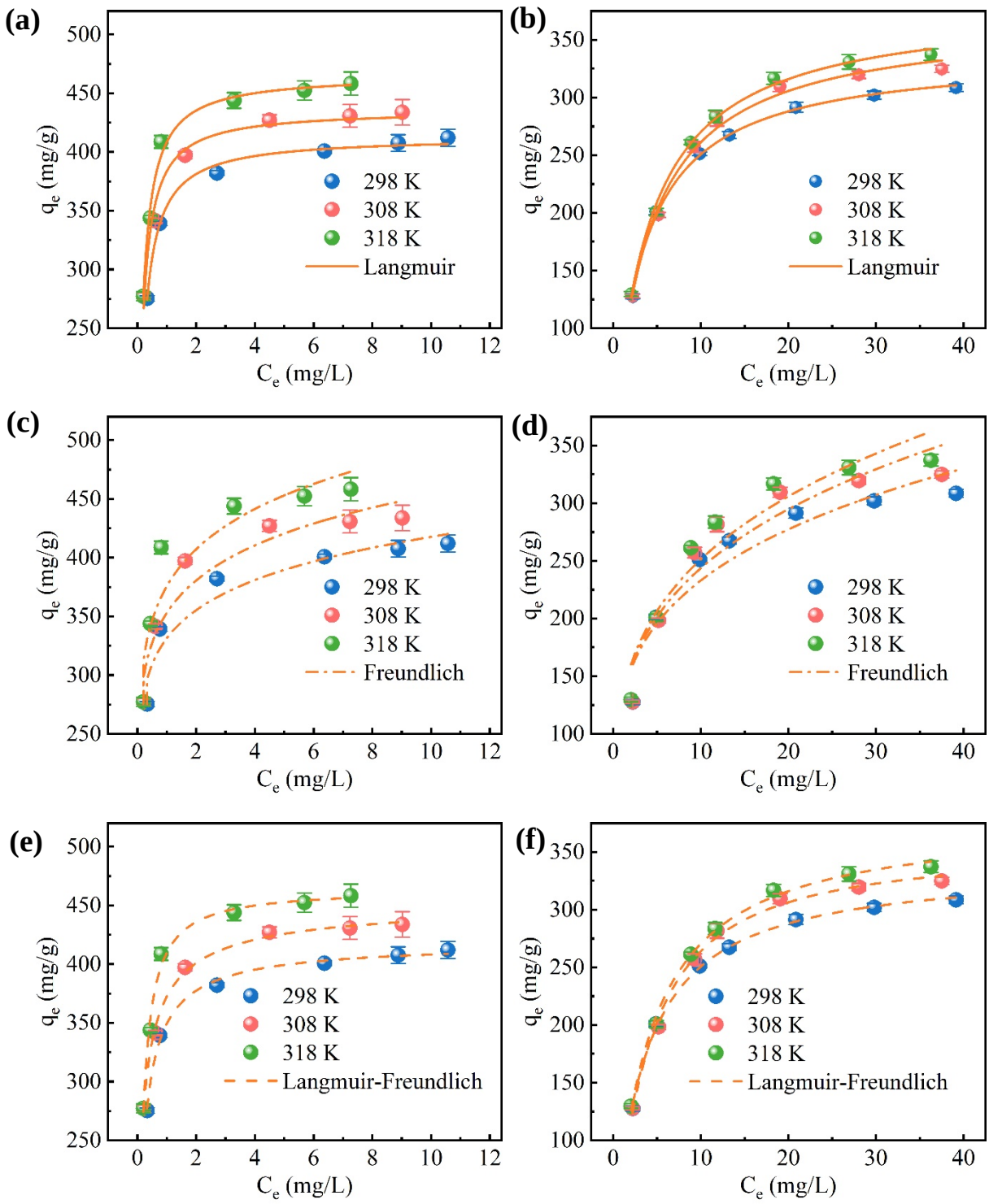

Figure 6. Adsorption isotherms for SDZ on Co_{SA}-CNF at temperatures of 298, 308 and 318 K fitted with (a) Langmuir, (c) Freundlich, and (e) Langmuir-Freundlich models ([SDZ]=10−40 mg/L, [adsorbent]=0.1 g/L, pH without pre-adjustment); adsorption isotherms for ROX on Co_{SA}-CNF at temperatures of 298, 308 and 318 K fitted with (b) Langmuir, (d) Freundlich, and (f) Langmuir-Freundlich models ([ROX]=10−60 mg/L, [adsorbent]=0.1g/L, pH without pre-adjustment).

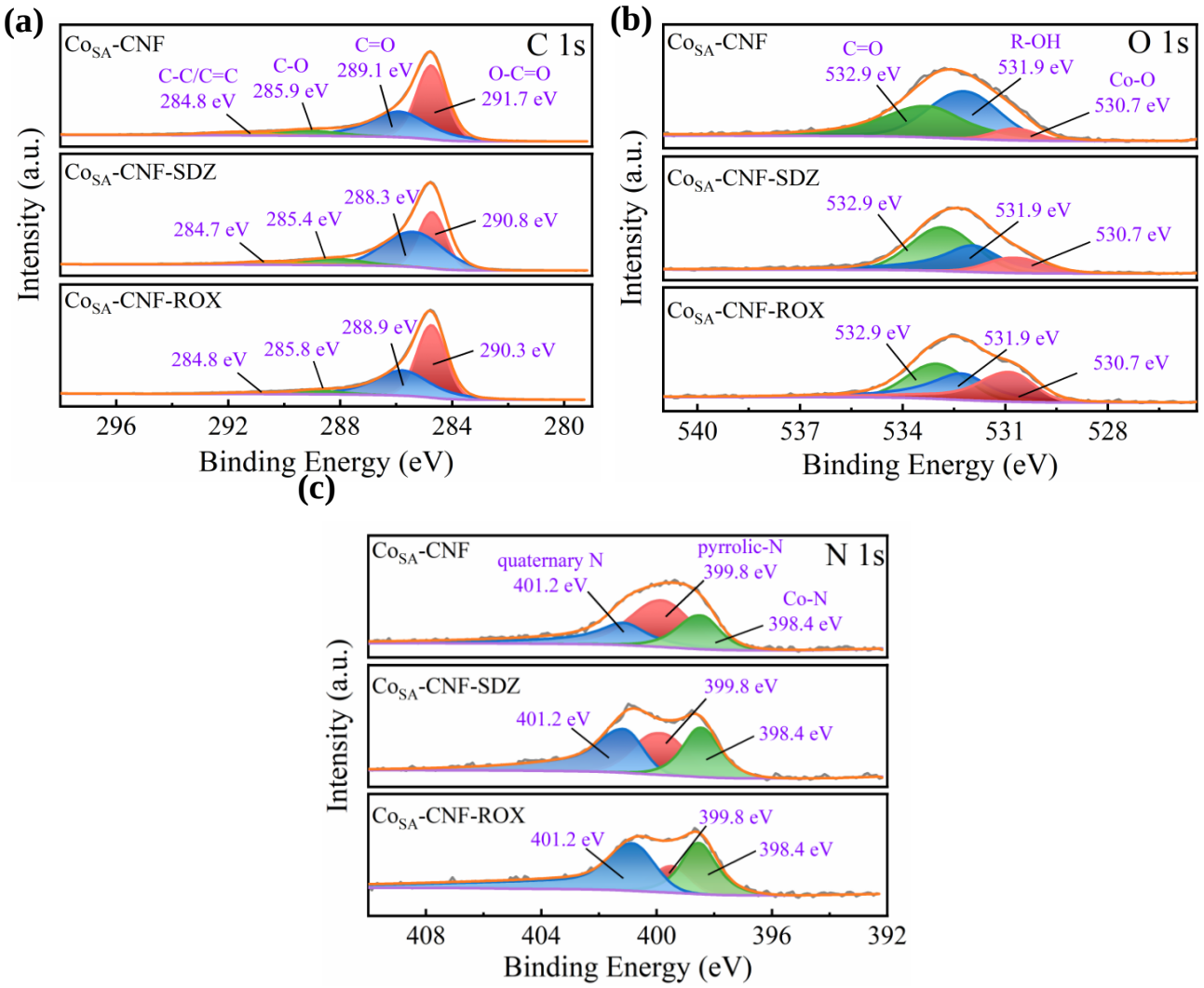

Figure 7. High-resolution XPS spectrum of (a) C 1s, (b) O 1s and (c) N 1s of Co_{SA}-CNF before and after adsorption of SDZ and ROX.

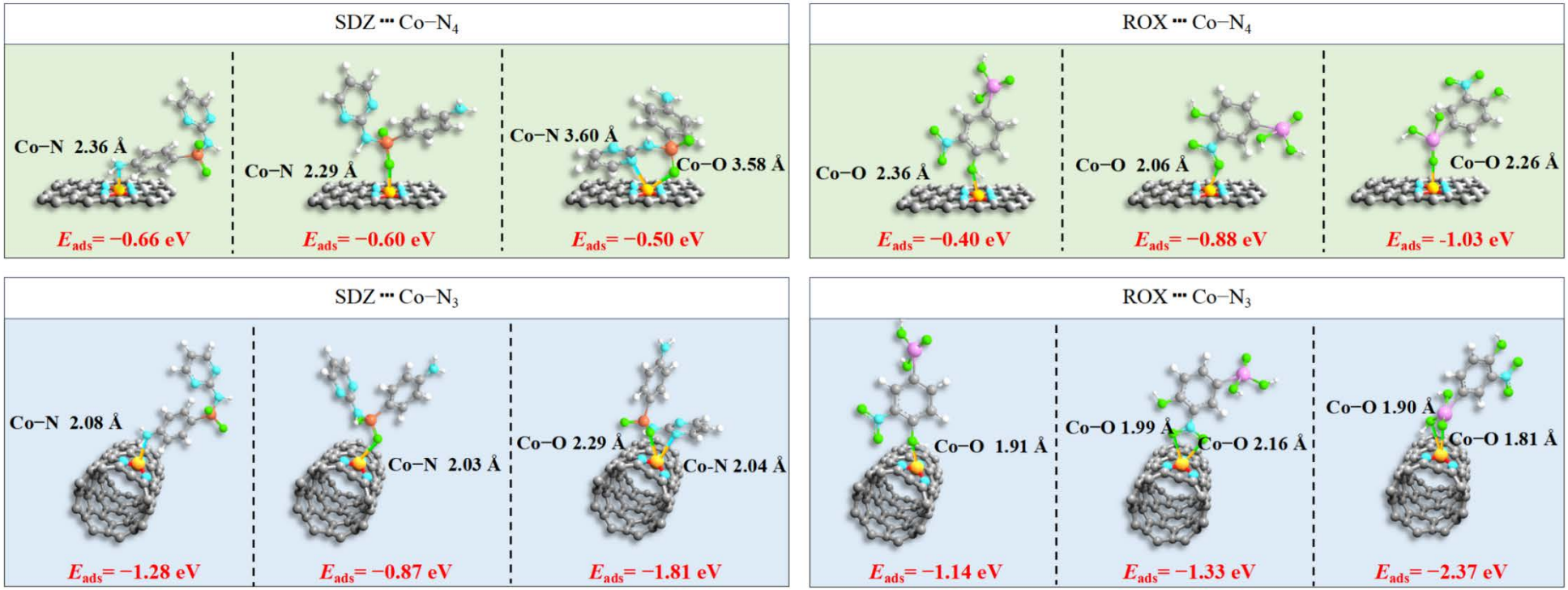

Figure 8. Optimized adsorption complexes of SDZ and ROX onto Co_{SA}-CNF at $Co{-}N_4$ and $Co{-}N_3$ sites (black, yellow, blue, green, orange, magenta, and white balls denote C, Co, N, O, S, As, and H atoms, respectively).

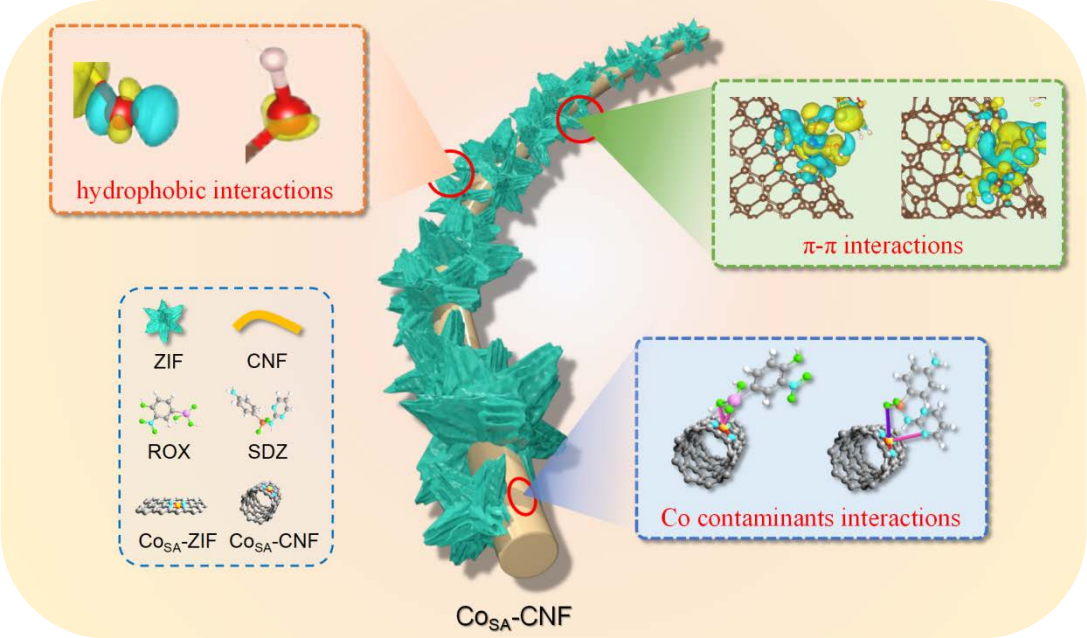

Figure 9. Proposed mechanisms of SDZ and ROX adsorption on Co_{SA}-CNF.

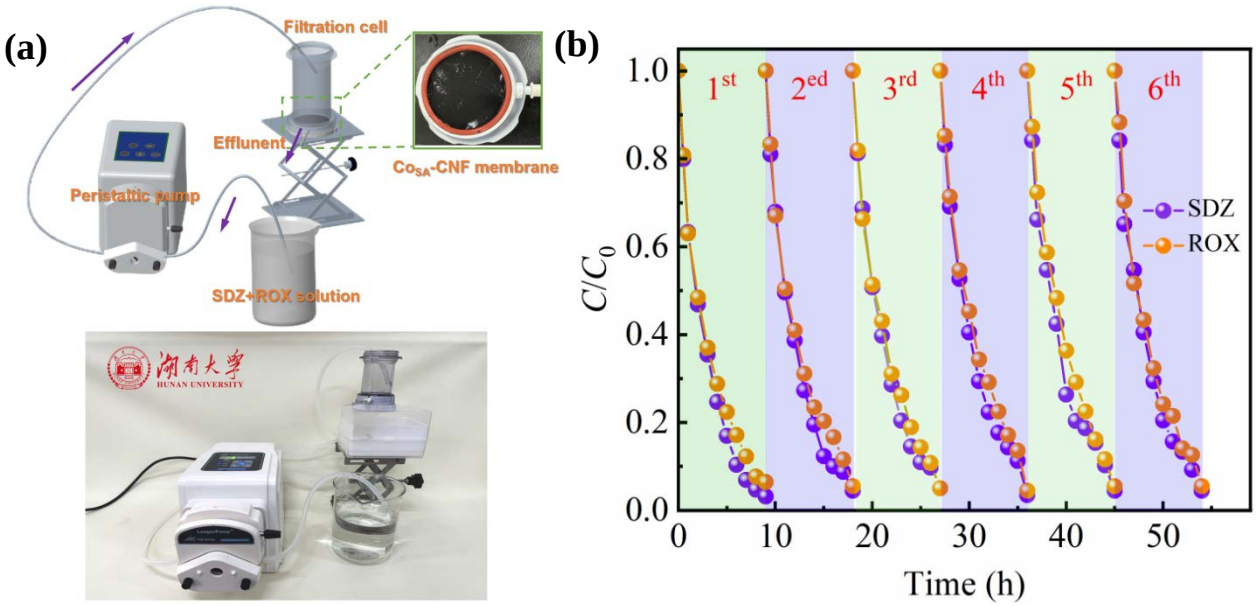

Figure 10. (a) The schematic diagram and photograph of the continuous flow filtration cell; (b) Recyclability of the Co_{SA}-CNF membrane in a continuous flow filtration cell ([SDZ]=[ROX]=10 mg/L, membrane weight: 12 mg, *T*=298 K, flow rate: 1.39±0.1 mL/min).

Supplementary information

for

In situ grown single-atom cobalt on carbon nanofibers for efficient adsorptive removal of organic pollutants: performance and mechanisms understanding

Simeng Xia[a,b], Fan Chen[a,b], Zhou Shi[a,b], Lin Deng[a,b,*], Anett Georgi[c], Haojie Zhang[c,*]

a. Hunan Engineering Research Center of Water Security Technology and Application, College of Civil Engineering, Hunan University, Changsha 410082, China

b. Key Laboratory of Building Safety and Energy Efficiency, Ministry of Education, College of Civil Engineering, Hunan University, Changsha 410082, China

c. Helmholtz Centre for Environmental Research-UFZ, Department of Technical Biogeochemistry, Leipzig 04318, Germany

*Corresponding authors

E-mail addresses: lindeng@hnu.edu.cn (L. Deng); haojie.zhang@ufz.de (H. Zhang)

This supplementary material includes 35 pages, 5 Texts, 18 Figures, 9 Tables, and 17 references.

Contents

Figure S13. Effects of (a) Na^+, (b) K^+, (c) Mg^{2+}, and (d) Ca^{2+} and (e) HA on the adsorption of ROX by Co_{SA}-CNF, and (e) the corresponding K_d values.

Figure S14. (a) XRD patterns, (b) FTIR spectroscopy, and (c) Raman spectra of Co_{SA}-CNF before and after adsorption of SDZ and ROX.

Figure S15. N_2 adsorption-desorption isotherms and pore size distributions of (a) Co_{SA}-CNF-SDZ and (b) Co_{SA}-CNF-ROX.

Figure S16. Molecular structures of (a) SDZ and (b) ROX.

Figure S17. The top view, side view and charge density difference of optimized adsorption complexes of SDZ onto Co_{SA}-CNF at $Co{-}N_4$ and $Co{-}N_3$ sites.

Figure S18. The top view, side view and charge density difference of optimized adsorption complexes of ROX onto Co_{SA}-CNF at $Co{-}N_4$ and $Co{-}N_3$ sites.

Table S1. EXAFS fitting parameters at the Co K-edge.

Table S2. Textural properties of CNF, Co_{SA}, ZIF, and Co_{SA}-CNF.

Table S3. Peaks information of C 1s, O 1s and N 1s.

Table S4. Parameters of pseudo-first-order and pseudo-second-order kinetic models for adsorption of SDZ and ROX onto Co_{SA}-CNF.

Table S5. Langmuir, Freundlich, and Langmuir-Freundlich constants for SDZ and ROX adsorption on Co_{SA}-CNF.

Table S6. Comparison in adsorption capacity of Co_{SA}-CNF toward SDZ with other reported adsorbents.

Table S7. Comparison in adsorption capacity of Co_{SA}-CNF toward ROX with other reported adsorbents.

Table S8. Thermodynamic parameters for SDZ and ROX adsorption onto Co_{SA}-CNF.

Table S9. Textural properties of the fresh and used Co_{SA}-CNF composites.

Text S1. Characterizations

The surface morphology, crystal structure of the samples were recorded with X-ray diffraction (XRD, D8 Advance X-ray diffract meter) equipped with Ni-filtered Cu Kα radiation at a scan rate (2θ) of 0.02°/s, scanning electron microscopy (SEM, JEOLJSM-7900F), high resolution transmission electron microscopy (HRTEM, JEM-2100F), and energy-dispersive X-ray spectroscopy (EDX, JEM 2100F). The Brunauer-Emmett-Teller (BET) specific surface area was measured through analyzing the N_2 adsorption-desorption isotherm at 77 K (ASAP 2010, Micromeritics Co.). X-ray photoelectron spectroscopy (XPS) was performed using an ESCALAB 250 apparatus (Thermo Fisher Scientific) at 3×10^{-10} mbar using Al Kα X-ray beams. Fourier transform infrared spectroscopy (FTIR) was collected on a total reflection infrared spectrometer (Thermo Fisher Scientific, Nicolet-6700). Raman spectra was recorded on a Horiba Jobin Yvon LabRam instrument with a HeNe laser excitation at 633 nm. Zeta potential was recorded using the Zetasizer Nano ZS (Malvern Instruments, UK). The X-ray absorption spectra (XAS) of Co K-edge were measured at the XRD station of beamline 4B9A of Beijing Synchrotron Radiation Facility (BSRF) in transmission mode. XANES and EXAFS data reduction and analysis were processed by Athena software. Element content analysis of the samples was carried out on inductively coupled plasma mass spectrometer (ICP-OES, Agilent 7800MS).

Text S2. Analytical methods

The concentration of organic pollutants was detected using a high-performance liquid chromatography (HPLC, Agilent 1260, USA) equipped with a IC-C18(2) column, The column temperature was set at 25℃, the mobile phase flow rate was 1.0 mL/min and the injection volume was 20 μL. The specific parameters were as follows, ***SDZ***: the determination wavelength was 270 nm and the mobile phase was methanol:water (55:45, V:V); ***ROX***: the determination wavelength was 264 nm and the mobile phase was composed of 0.1 % formic acid: methanol (60:40, V:V); ***SMX***: the determination wavelength was 269 nm and the mobile phase was methanol:water (53:47, V:V); ***CBZ***: the determination wavelength was 280 nm and the mobile phase was methanol:water (80:20, V:V); ***CM***: the determination wavelength was 277 nm and the mobile phase was methanol:water (55:45, V:V); ***APAP***: the determination wavelength was 250 nm and the mobile phase was methanol:water (55:45, V:V); ***BA***: the determination wavelength was 227 nm and the mobile phase was methanol: ammonium acetate (35:65, V:V). Atomic absorption spectrophotometry (AA-6880, Shimadzu) was used to determine Co^{2+} concentrations leached from the adsorbents.

Text S3. The equations of pseudo-first-order, pseudo-second-order, and intraparticle diffusion models

Pseudo-first-order model:

$$q_t=q_e(1-e^{-k_1t}) \qquad \text{(S1)}$$

Pseudo-second-order model:

$$q_t=q_e\left(1-\frac{1}{1+q_ek_2t}\right) \qquad \text{(S2)}$$

where q_t (mg/g) and q_e (mg/g) represent the adsorbed amount of SDZ and ROX at time t and equilibrium, k_1 (1/min) and k_2 (g/(mg·min)) are the corresponding rate constants of the pseudo-first-order and pseudo-second-order, respectively.

Text S4. The equations of Langmuir, Freundlich, and Langmuir-Freundlich models

Langmuir model

$$q_e = \frac{q_m \cdot K_L \cdot C_e}{1 + K_L \cdot C_e} \qquad \text{(S3)}$$

Freundlich model:

$$q_e = K_F \cdot C_e^{1/n} \qquad \text{(S4)}$$

Langmuir- Freundlich model:

$$q_e = \frac{k_{LF} C_e^{1/n_{LF}}}{1 + C_e^{1/n_{LF}}} \qquad \text{(S5)}$$

where q_e and q_m (mg/g) are the adsorbed amount at equilibrium and the maximum adsorption capacity of the monolayer, C_e (mg/L) is the SDZ and ROX concentration at equilibrium, K_L (L/mg), K_F ($mg^{1-(1/n)}$ $L^{1/n}$ g^{-1}), K_{LF}((mg/g) • (mg/L)^{nLF}), and a_{LF} ((mg/L)^{nLF}) are the corresponding adsorption equilibrium constant, $1/n$ is the Freundlich exponent, and n_{LF} is the heterogeneity parameter.

Text S5. Thermodynamic parameters determination

The thermodynamic parameters such as the changes in standard Gibbs energy (ΔG^0, kJ/mol), standard enthalpy (ΔH^0, kJ/mol) and standard entropy (ΔS^0, J/(mol·K)) were calculated using Eqs. (S6)-(S9).

$$\Delta G^0 = \Delta H^0 - T\Delta S^0 \tag{S6}$$

$$\Delta G^0 = -RT \ln K^o \tag{S7}$$

$$K^o[-] = K_L \left[\frac{L}{mg}\right] \times C_{ref,solute} \left[\frac{mol}{L}\right] \times MW_{solute}[mg/mol] \tag{S8}$$

$$\ln K^0 = \frac{\Delta S^0}{R} - \frac{\Delta H^0}{RT} \tag{S9}$$

where K^O is the dimensionless equilibrium constant, K_L (L/mg) is the adsorption equilibrium constant fitted by Langmuir model, *MWsolute* is the molecular weight of the solute and $C_{ref,solute}$ is the solute concentration of the reference state for the dissolved solute ($C_{ref,solute}$ = 1 mol/L), T (K) is the absolute temperature, and R (8.314 J/(K·mol)) is the universal gas constant. By using eq. S8 for the conversion of the Langmuir constant (L/mg) into the dimensionless K^O we follow the approach suggested by Zhou and Zhou (2014, their equation 13) [S1] which is based on the derivation of the Langmuir model from chemical potentials. This conversion is needed to solve the unit problem in calculating thermodynamic parameters. Note that according to mathematical rules a logarithm can only be formed from unitless parameters.

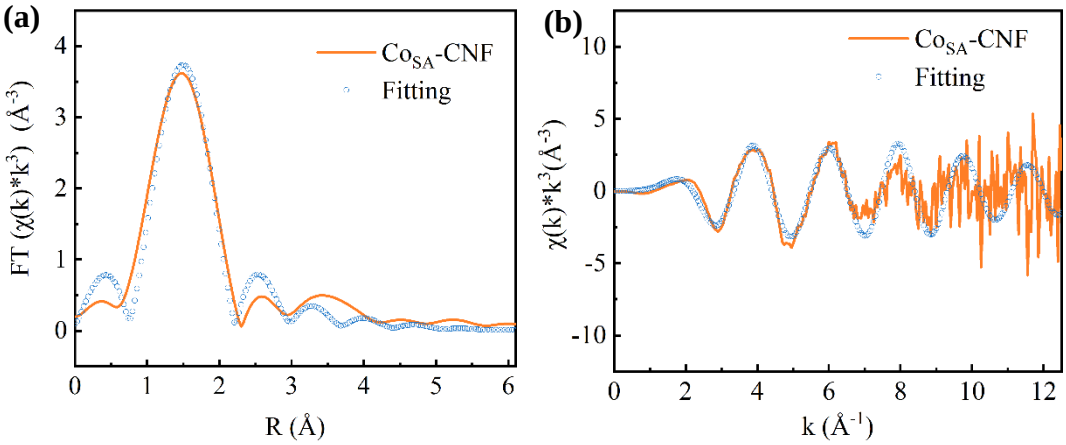

Figure S1. Corresponding EXAFS fitting curves at (a) *R* and (b) *k* space.

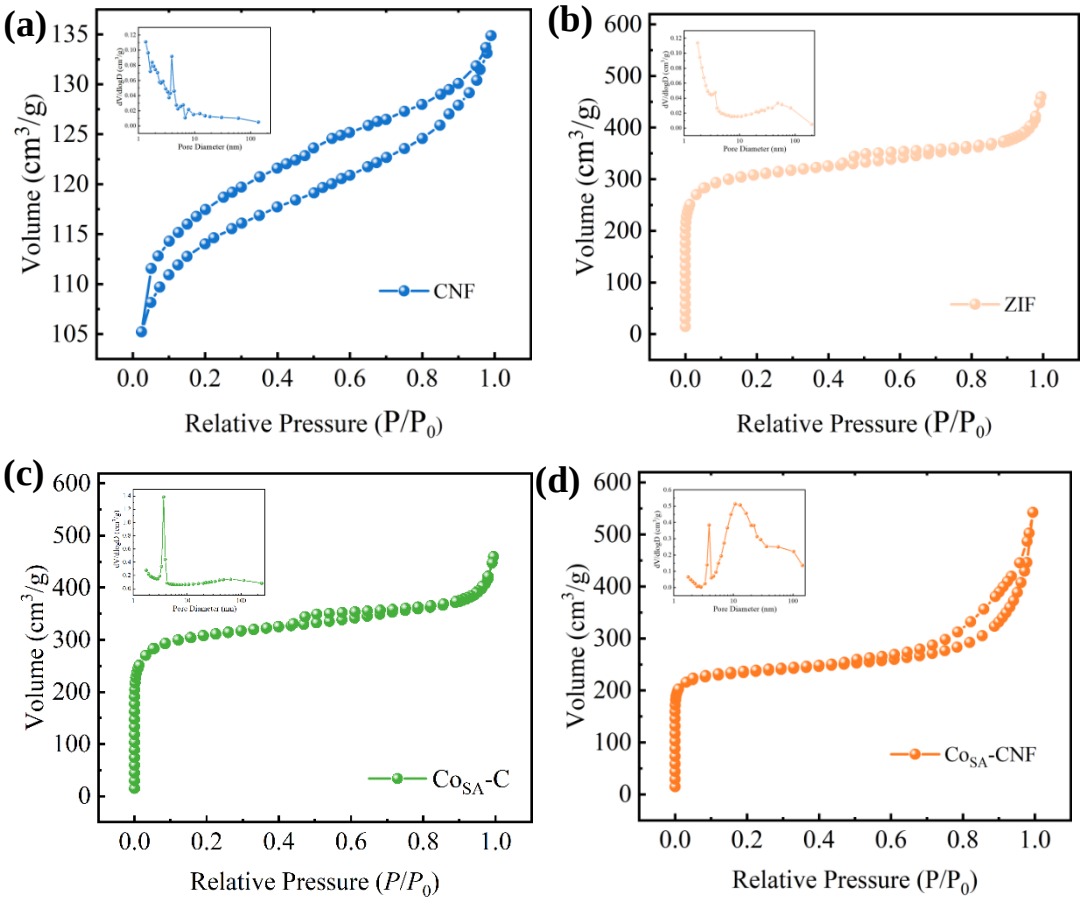

Figure S2. N_2 adsorption-desorption isotherms and pore size distributions of (a) CNF, (b) ZIF, (c) Co_{SA}-C, and (d) Co_{SA}-CNF.

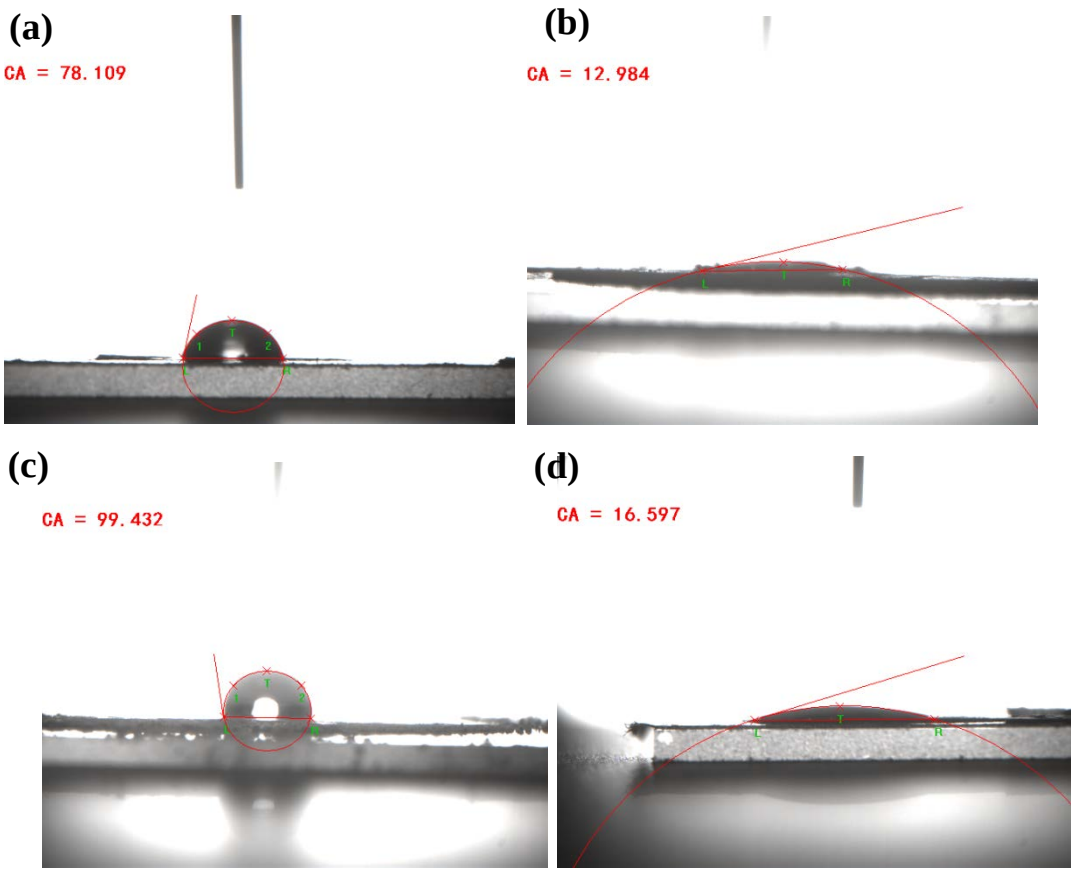

Figure S3. Contact angle tests for (a) CNF, (b) Co_{SA}-C, (c) ZIF, and (d) Co_{SA}-CNF.

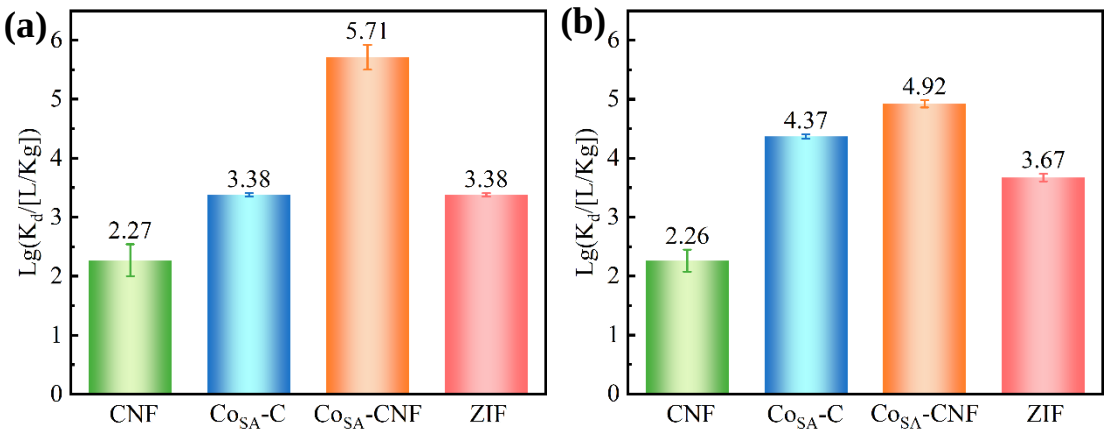

Figure S4. LgK_d values for (a) SDZ and (b) ROX adsorption on various adsorbents; ([SDZ]=[ROX]=10 mg/L, pH without pre-adjustment, [adsorbent]=0.1g/L, T=298 K).

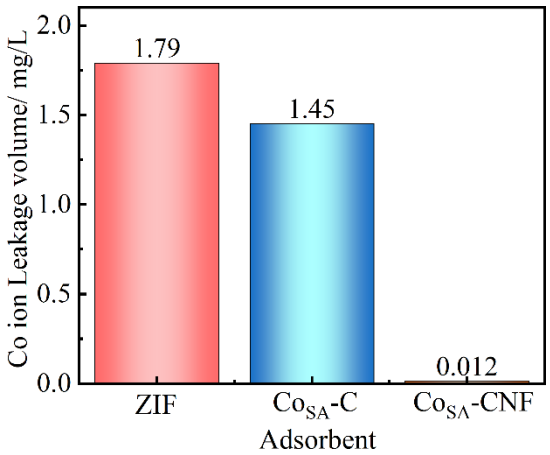

Figure S5. Co ion leaching from ZIF, Co$_{SA}$-C, and Co$_{SA}$-CNF. ([SDZ]= 10 mg/L, pH without pre-adjustment, [adsorbent]=0.1g/L, *T*=298 K).

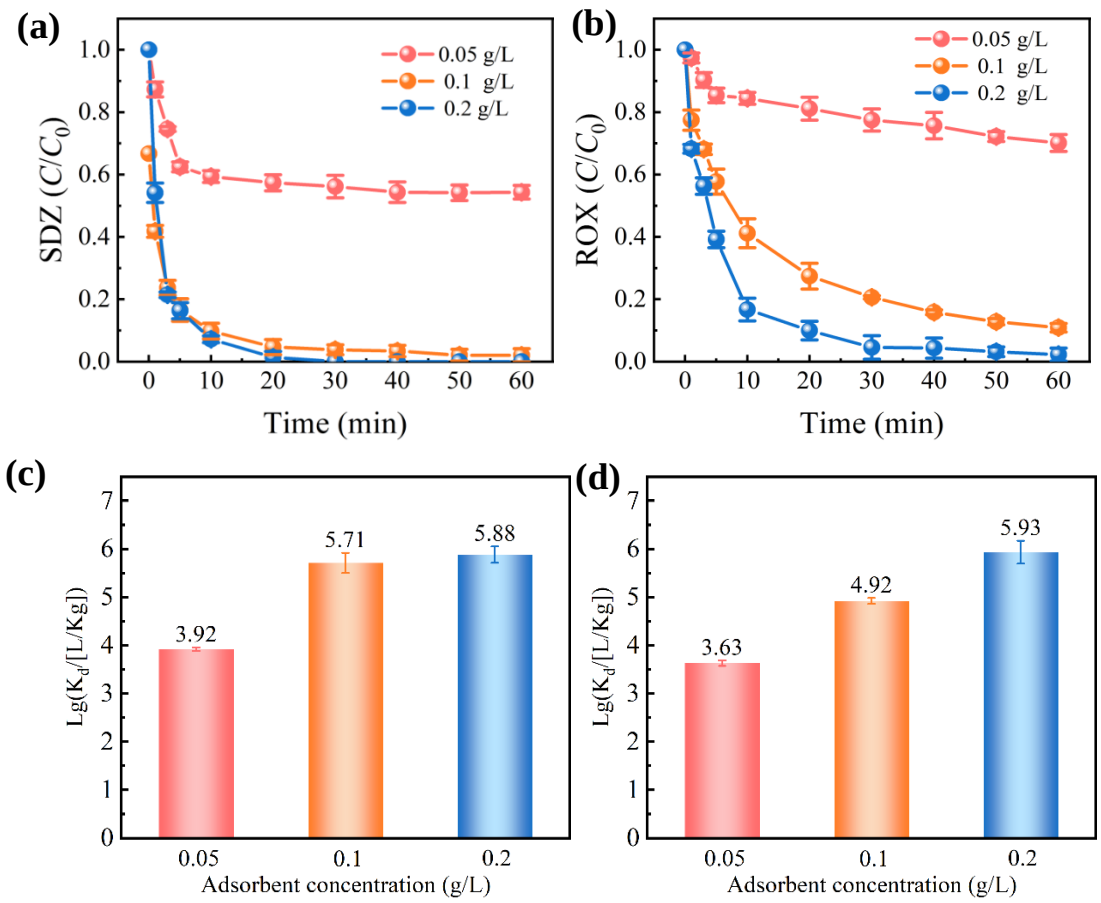

Figure S6 effect of adsorbent concentration on (a) SDZ and (b) ROX removal by Co_{SA}-CNF ([SDZ]=[ROX]=10 mg/L, pH without pre-adjustment, T=298 K); LgK_d values for (c) SDZ and (d) ROX adsorption by Co_{SA}-CNF at different adsorbent concentrations;

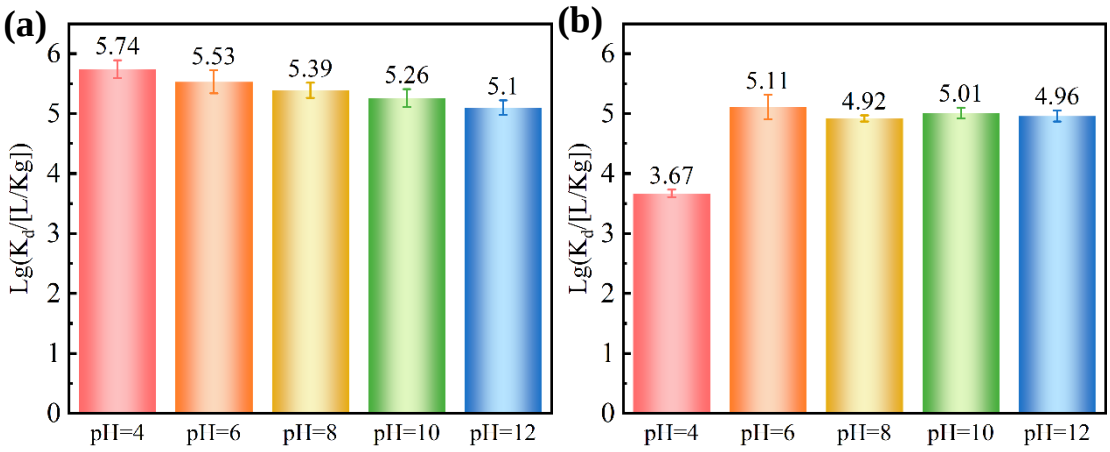

Figure S7. LgK_d values for (e) SDZ and (f) ROX adsorption by Co_{SA}-CNF at different pH. ([SDZ]=[ROX]=10 mg/L, [adsorbent]=0.1g/L, T=298 K)

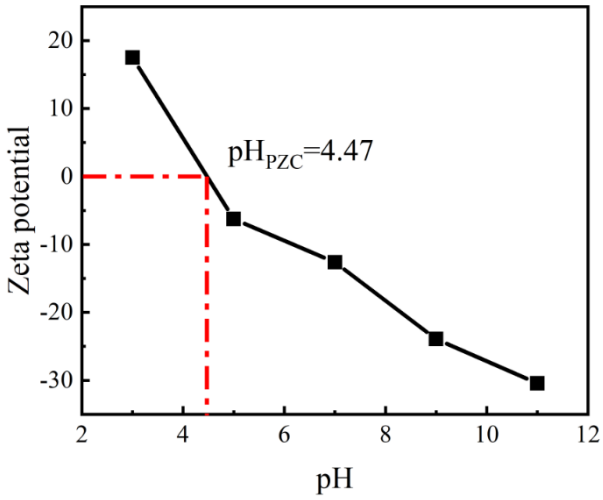

Figure S8. pH$_{PZC}$ determination of Co$_{SA}$-CNF.

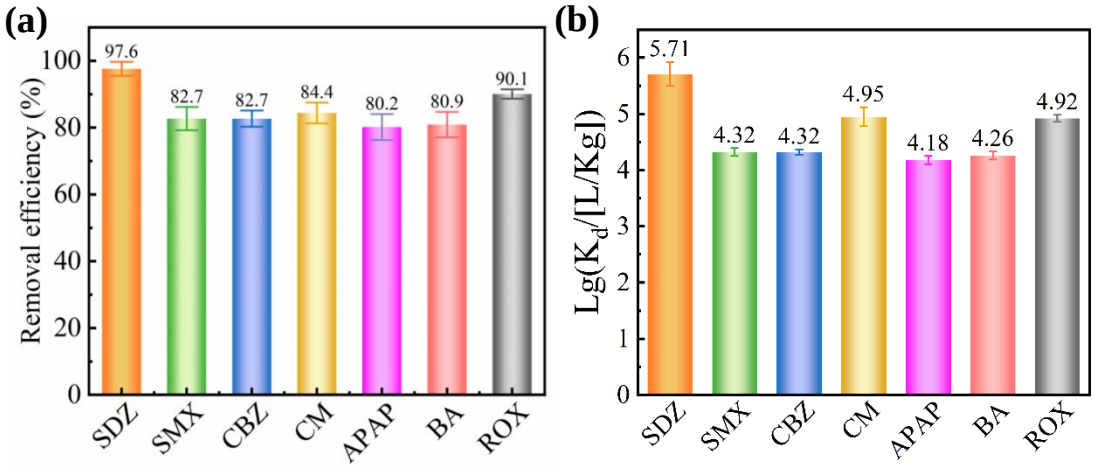

Figure S9. (a) Adsorption of various organic contaminants using Co_{SA}-CNF, and (b) corresponding K_d values ([Pollutants]=10 mg/L, [adsorbent]= 0.1 g/L, pH without pre-adjustment, T=298 K, reaction time: 60 min).

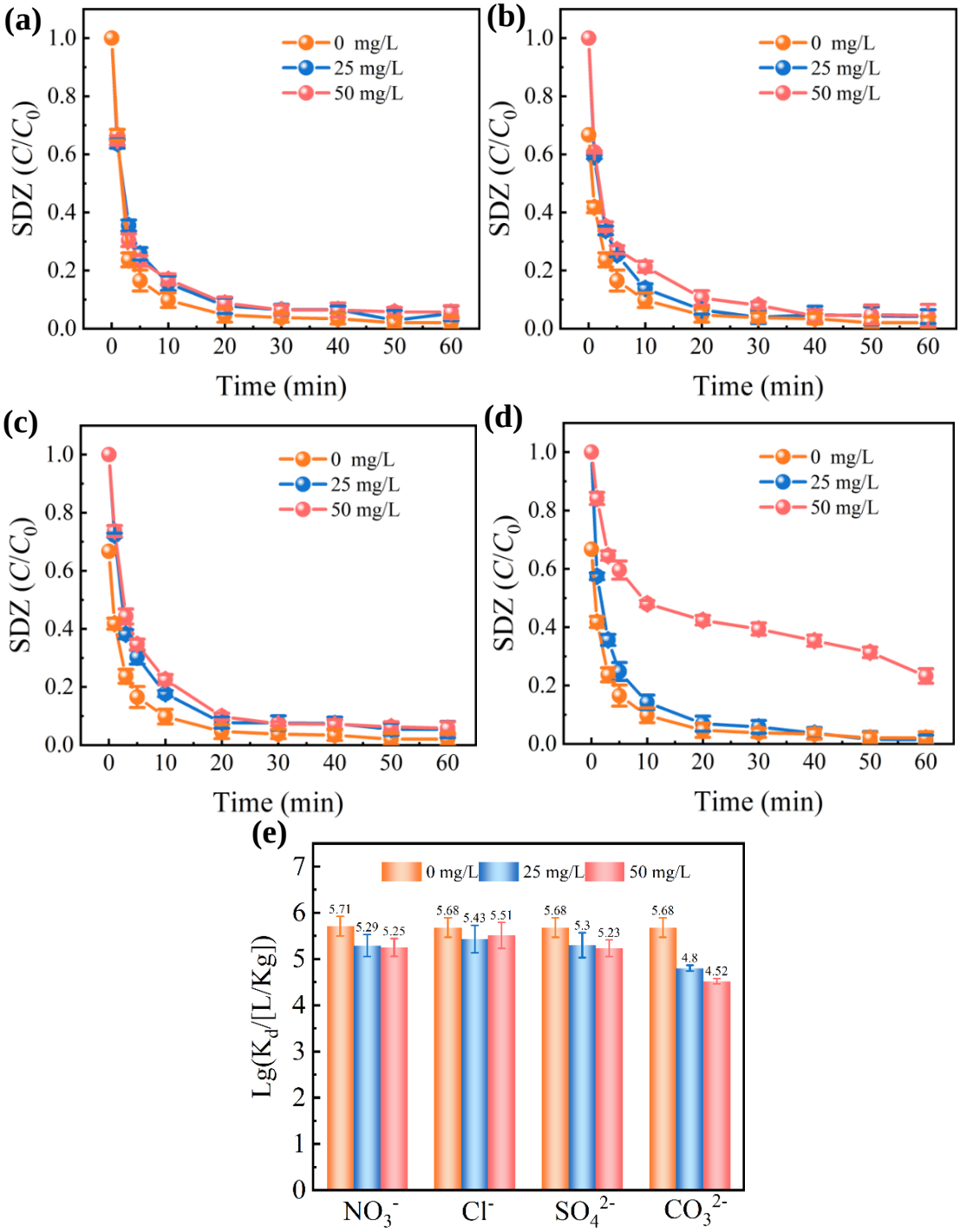

Figure S10. Effects of (a) NO_3^-, (b) Cl^-, (c) SO_4^{2-}, and (d) CO_3^{2-} on the adsorption of SDZ by Co_{SA}-CNF, and (e) the corresponding K_d values ([SDZ]=10 mg/L, [adsorbent]= 0.1 g/L, pH without pre-adjustment, T=298 *K*).

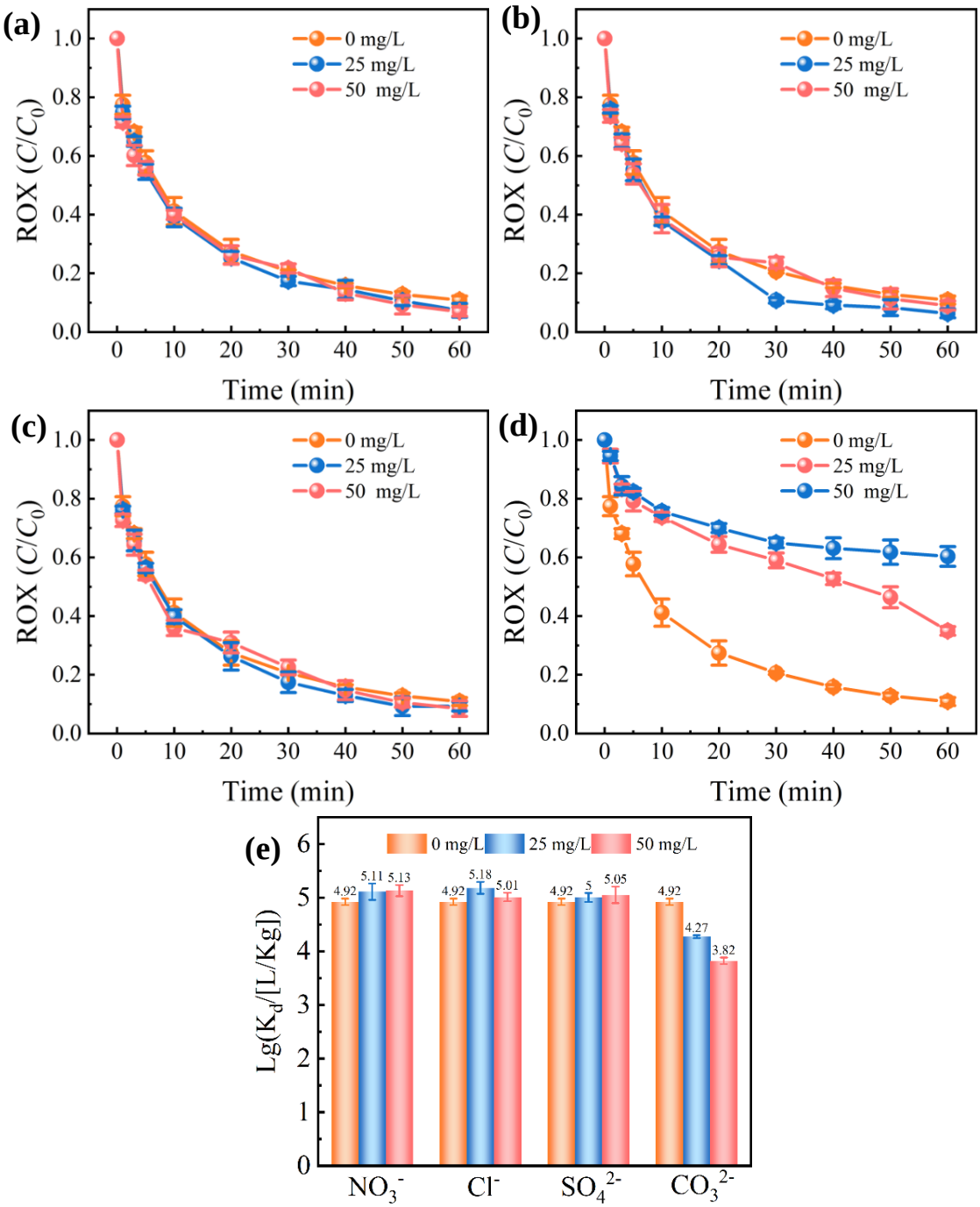

Figure S11. Effects of (a) NO_3^-, (b) Cl^-, (c) SO_4^{2-}, and (d) CO_3^{2-} on the adsorption of ROX by Co_{SA}-CNF, and (e) the corresponding K_d values ([ROX]=10 mg/L, [adsorbent]= 0.1 g/L, pH without pre-adjustment, T = 298 K).

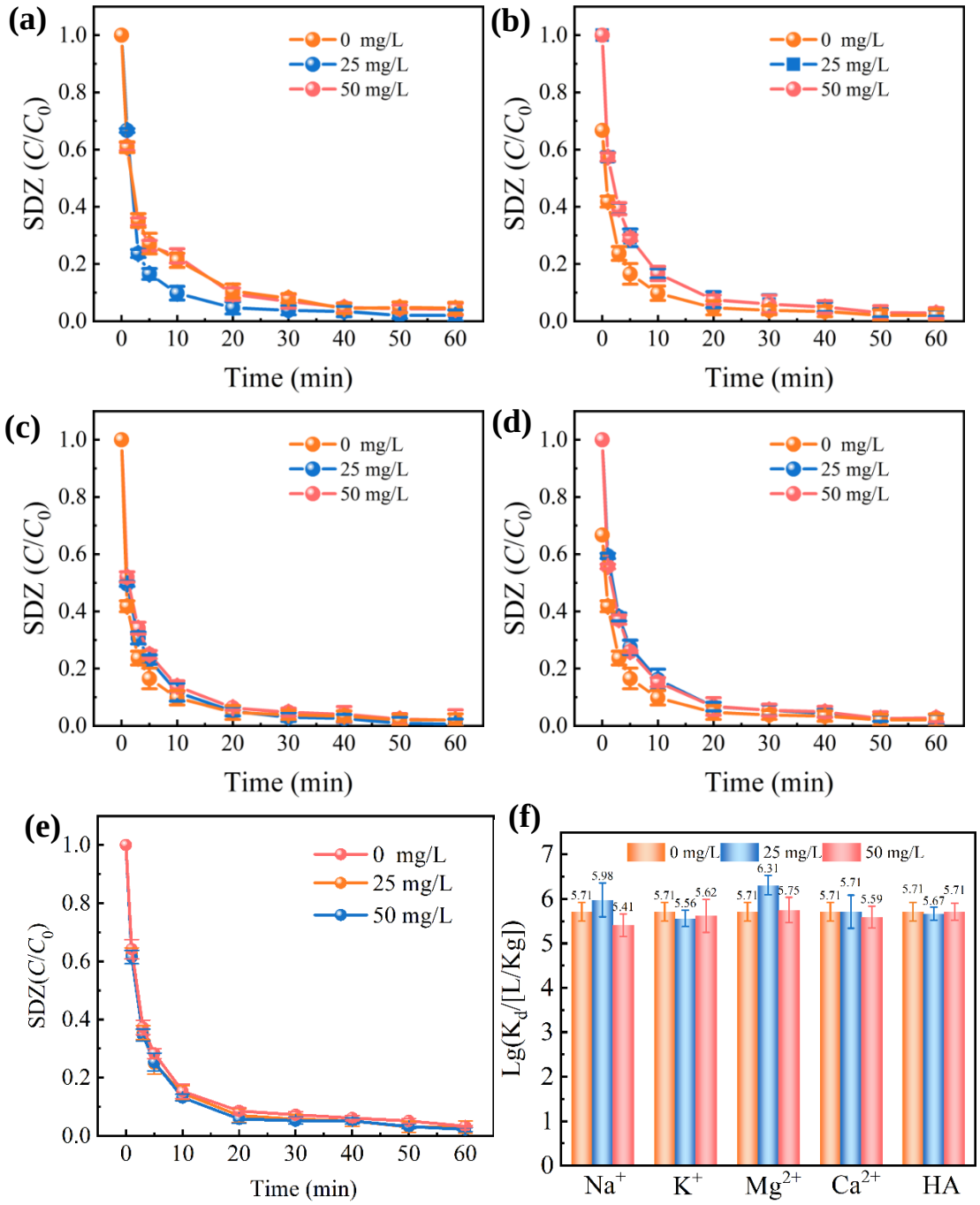

Figure S12. Effects of (a) Na^+, (b) K^+, (c) Mg^{2+}, (d) Ca^{2+} and (e) HA on the adsorption of SDZ by Co_{SA}-CNF, and (e) the corresponding K_d values ([SDZ]=10 mg/L, [adsorbent]= 0.1 g/L, pH without pre-adjustment, T=298 K).

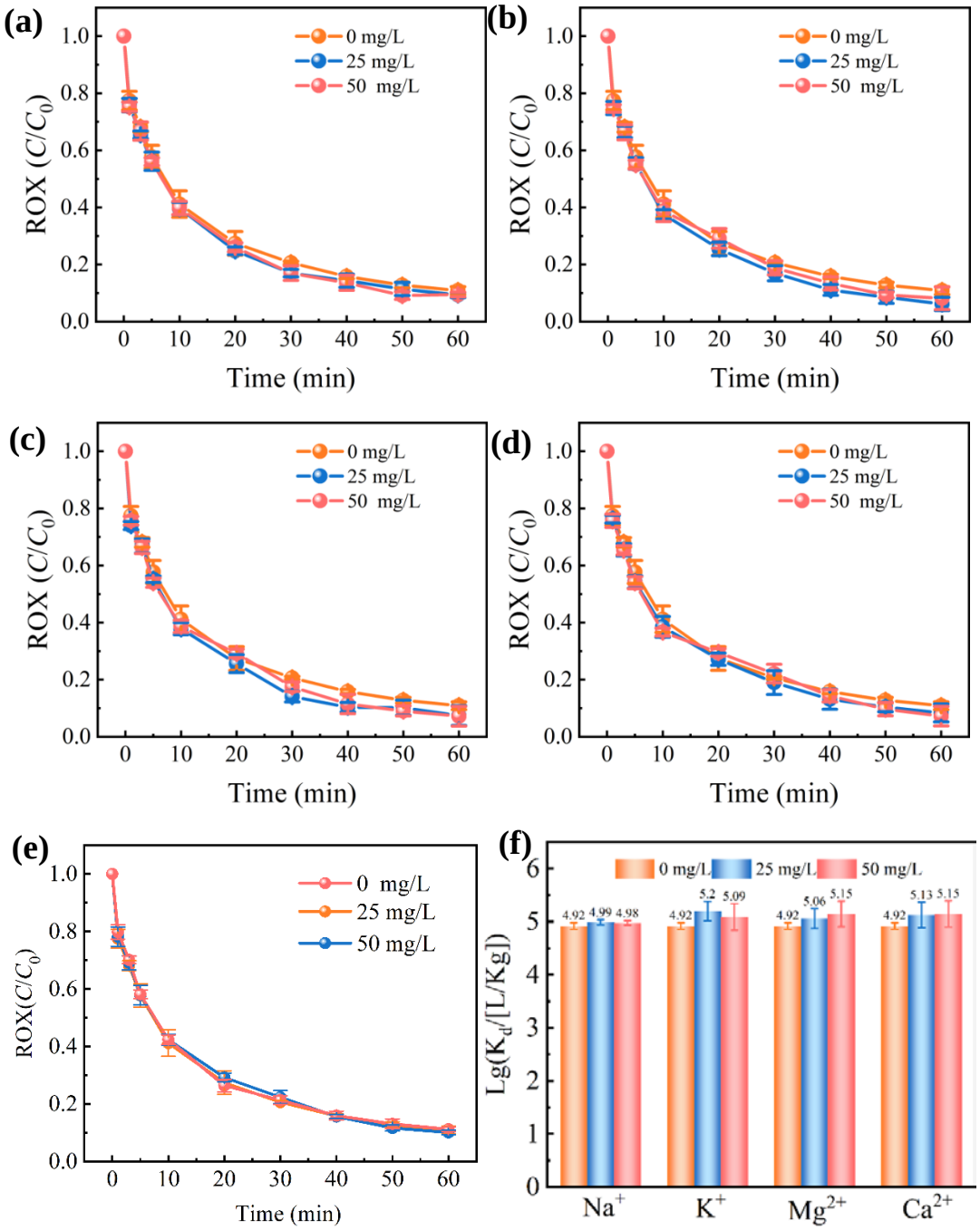

Figure S13. Effects of (a) Na^+, (b) K^+, (c) Mg^{2+}, (d) Ca^{2+} and (e) HA on the adsorption of ROX by Co_{SA}-CNF, and (f) the corresponding K_d values ([ROX]=10 mg/L, [adsorbent]=0.1 g/L, pH without pre-adjustment, T=298 K).

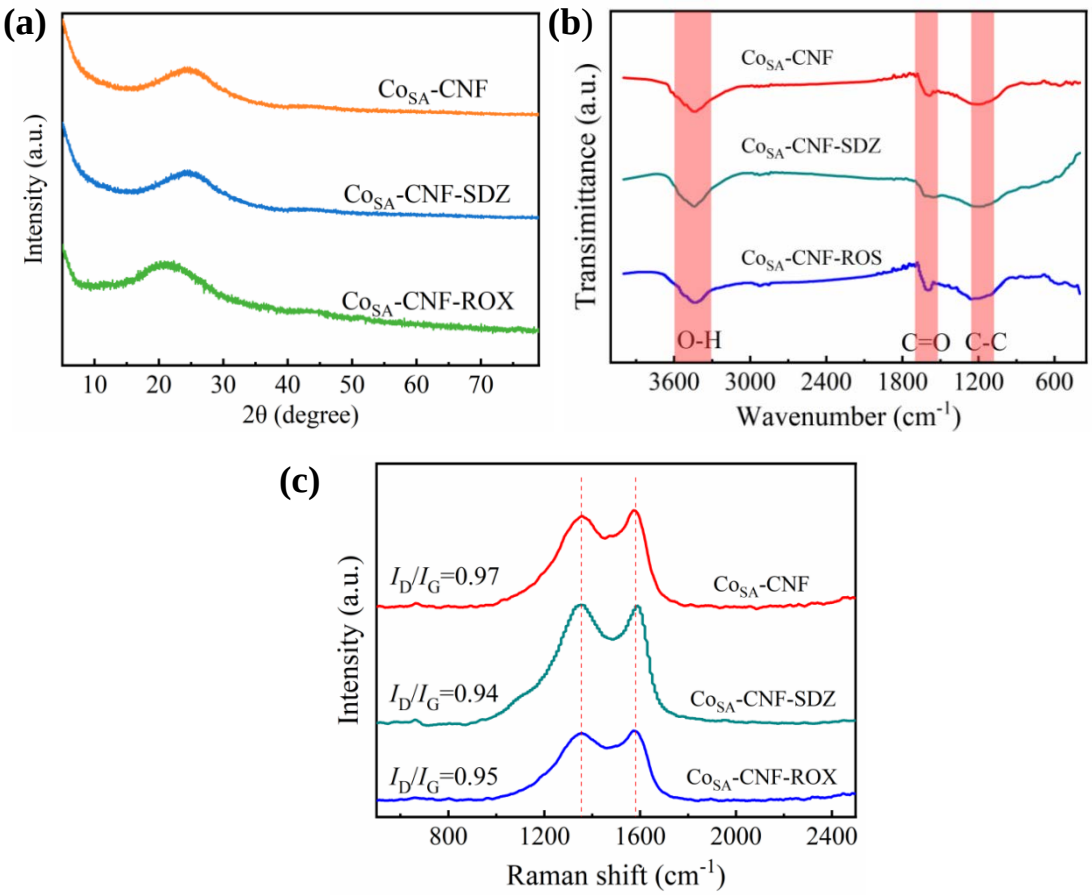

Figure S14. (a) XRD patterns, (b) FTIR spectroscopy, and (c) Raman spectra of Co_{SA}-CNF before and after adsorption of SDZ and ROX.

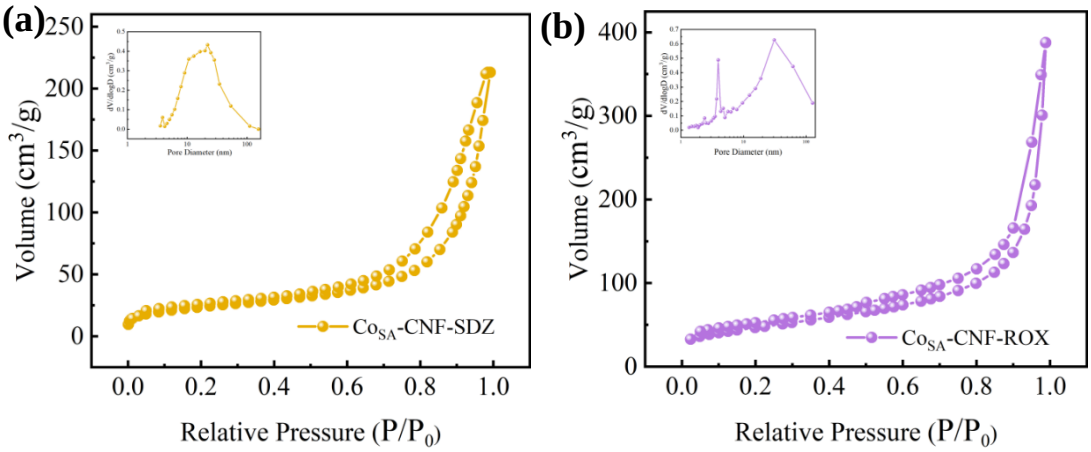

Figure S15. N_2 adsorption-desorption isotherms and pore size distributions of (a) Co_{SA}-CNF-SDZ and (b) Co_{SA}-CNF-ROX.

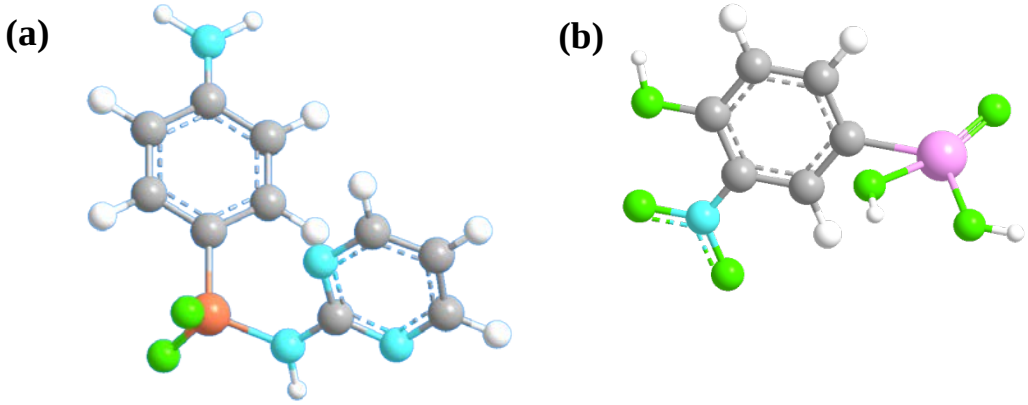

Figure S16. Molecular structures of (a) SDZ and (b) ROX.

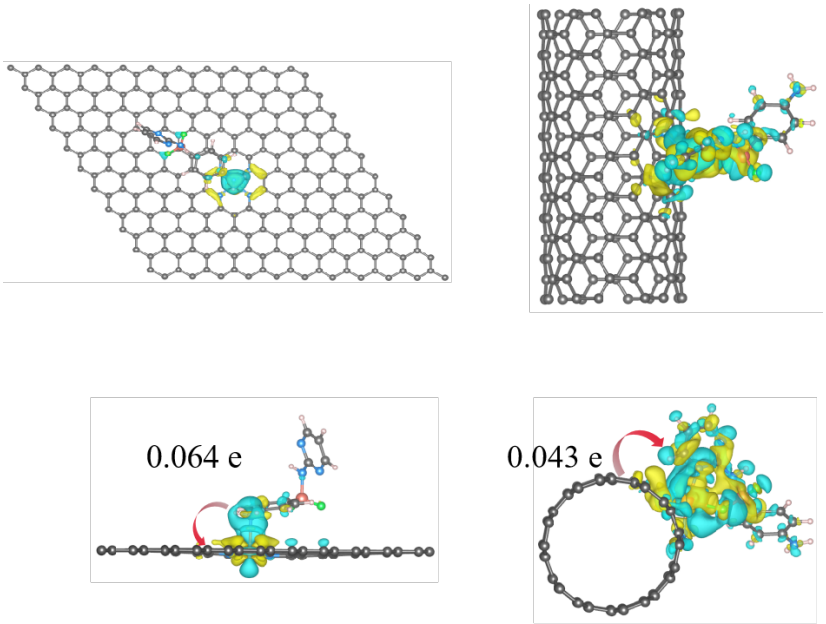

Figure S17. The top view, side view and charge density difference of optimized adsorption complexes of SDZ onto Co_{SA}-CNF at $Co{-}N_4$ and $Co{-}N_3$ sites.

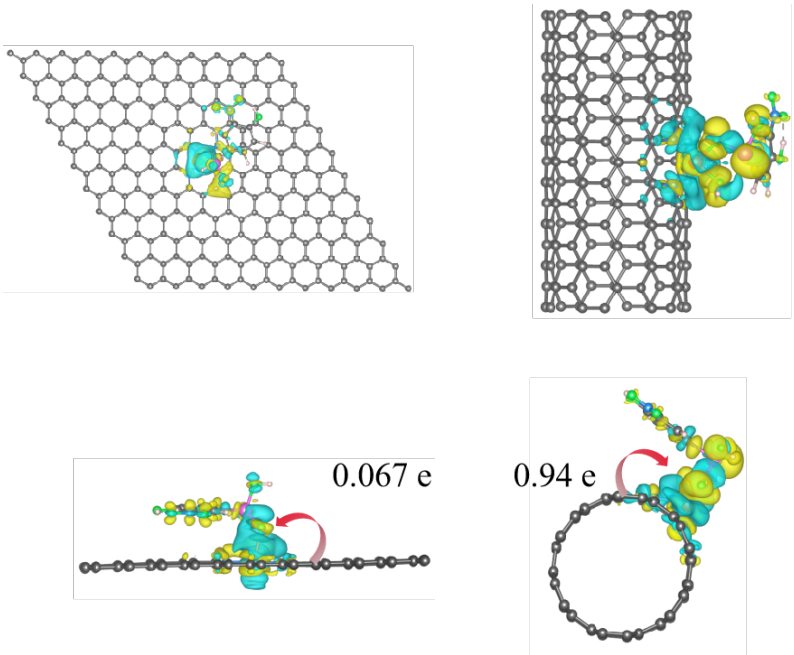

Figure S18. The top view, side view and charge density difference of optimized adsorption complexes of ROX onto Co_{SA}-CNF at $Co{-}N_4$ and $Co{-}N_3$ sites.

Table S1. EXAFS fitting parameters at the Co K-edge.

Sample	Shell	N	R(Å)	δ^2(×10^{-3} Å^{-2})	Rf
Co foil	Co-Co	12	2.49	6.10	0.0017
Co_{SA}-CNF	Co-N	3.57	2.07	2.04±1.40	0.020

S_0 was set to 0.7352 with Co foil reference. Date ranges: $3.0 \leq k \leq 10$ Å^{-1}, $1.0 \leq R \leq 3.0$ Å. [a]Path: The path of Co-Co is from the crystal structure of Co foil (COD ID:7233775), the path of Co-N is from the crystal structure of Co-Pc COD ID: 1534891; [b]N: coordination numbers; [c]R: bond distance; [d]σ^2: Debye-Waller factors; [f]R factor: goodness of fit.

Table S2. Textural properties of CNF, Co_{SA}-C, ZIF, and Co_{SA}-CNF.

Samples	S_{BET} (m^2/g)	$S_{external}$ (m^2/g)	$V_{micropore}$ (cm^3/g)	$V_{mesopore}$ (cm^3/g)
CNF	348	36	0.15	0.06
Co_{SA}-C	960	258	0.36	0.32
ZIF	804	74	0.38	0.06
Co_{SA}-CNF	709	157	0.29	0.54

Table S3. Peaks information of C 1s, O 1s and N 1s.

		Binding energy (eV)	Relative content (%)		
			Co_{SA}-CNF	Co_{SA}-CNF-SDZ	Co_{SA}-CNF-ROX
C 1s	C-C/C=C	284.8	53.0	35.9	54.5
	C-O	285.9	36.7	49.8	39.1
	C=O	289.1	6.5	8.7	4.5
	O-C=O	291.7	3.8	5.6	1.9
O 1s	Co-O	530.7	7.4	14.7	32.5
	R-OH	531.9	46.3	37.0	33.7
	C=O	532.9	46.3	48.3	33.8
N 1s	Co-N	398.4	23.6	28.6	30.0
	Pyrrolic-N	399.8	49.1	31.0	19.6
	Quaternary-N	401.2	27.3	40.4	50.4

Table S4. Parameters of pseudo-first-order and pseudo-second-order kinetic models for adsorption of SDZ and ROX onto Co_{SA}-CNF.

Pollutant	C_0 (mg/L)	Pseudo-first-order			Pseudo-second-order		
		k_1 (min^{-1})	Q_e (mg/g)	R^2	k_2 (g/(mg • min))	Q_e (mg/g)	R^2
SDZ	3	1.40	29.5	0.992	0.10	30.1	0.998
	10	0.73	95.5	0.964	0.013	98.6	0.998
	30	0.11	238.3	0.90	0.00055	262.8	0.967
ROX	3	0.14	29.5	0.970	0.0066	31.7	0.984
	10	0.12	87.3	0.971	0.0019	94.8	0.991
	30	0.033	201.8	0.995	0.00015	241.7	0.998

Table S5. Langmuir, Freundlich, and Langmuir-Freundlich constants for SDZ and ROX adsorption on Co_{SA}-CNF.

Models	Parameters	SDZ			ROX		
		298 K	308 K	318 K	298 K	308 K	318 K
Langmuir	Q_m (mg/g)	413	436	466	338	368	381
	K_L (L/mg)	5.96	7.10	7.30	0.24	0.24	0.29
	R^2	0.992	0.975	0.988	0.998	0.992	0.995
Freundlich	K_F (mg/g)	331	353	376	130	131	131
	$1/n$	0.10	0.11	0.12	0.25	0.27	0.28
	R^2	0.906	0.903	0.837	0.892	0.881	0.907
Langmuir-Freundlich	K_{LF}((mg/g)·(mg/L)^{nLF})	2078	2007	3483	78	86	91
	a_{LF}((mg/L)^{nLF})	4.95	4.39	7.50	0.26	0.22	0.24
	R^2	0.994	0.995	0.985	0.999	0.993	0.995

Table S6. Comparison in adsorption capacity of Co_{SA}-CNF toward SDZ with other reported adsorbents.

Adsorbents	Adsorption capacity (mg/g)	Dosage (mg/mL)	*T* (K)	Isotherm models	Ref.
Activated carbon	382	0.40	298	Prausnitz-Radke	[S2]
Biochar	84	0.40	318	Freundlich	[S3]
PSSMA-functionalized-chitosan	214	0.50	318	Langmuir	[S4]
Zirconium-based metal–organic frameworks	280	0.17	298	Langmuir	[S5]
Vegetal powdered activated carbon	137	0.10	298	Freundlich	[S6]
β-cyclodextrin/dopamine hydrochloride-graphene oxide	152	0.15	308	Langmuir	[S7]
Phosphoric acid-modified biochars	139	0.10	298	Langmuir	[S8]
Hydroxylated multi-walled carbon nanotubes	103	1.00	318	Langmuir	[S9]
Co_{SA}-CNF	465.88	0.10	318	Langmuir-Freundlich	This work

Table S7. Comparison in adsorption capacity of Co_{SA}-CNF toward ROX with other reported adsorbents.

Adsorbents	Adsorption capacity (mg/g)	Dosage (mg/mL)	*T* (K)	Isotherm models	Ref.
Multi-walled carbon nanotubes	14	2.00	303	Freundlich	[S10]
Molecularly imprinted polymers	100	0.67	298	Langmuir -	[S11]
Nonmolecularly imprinted polymers	74	0.67	298	Langmuir	[S11]
Corncob-derived activated carbon	293	0.40	318	Sips	[S12]
Magnetic molecularly imprinted polymers	16	0.20	298	Langmuir	[S13]
Magnetic non-imprinted polymers	5	0.20	298	Langmuir	[S13]
Cellulose	7	2.33	295	Langmuir	[S14]
Goethite	19	2.33	295	Langmuir	[S14]
Goethite-cellulose (30%, Fe)	17	2.33	295	Langmuir	[S14]
Goethite-cellulose (30%, Fe)	12	2.33	295	Langmuir	[S14]
Goethite-cellulose (30%, Fe)	6	2.33	295	Langmuir	[S14]
Co_{SA}-CNF	380.74	0.10	318	Langmuir-Freundlich	This work

Table S8. Thermodynamic parameters for SDZ and ROX adsorption on Co_{SA}-CNF.

	ΔG^0 (kJ/mol)			ΔS^0 (J/(mol • K))	ΔH^0 (kJ/mol)
	298 K	308 K	318 K		
SDZ	−35.22	−36.85	−38.12	145.9	8.05
ROX	−27.38	−28.30	−29.72	116.37	7.37

Table S9. Textural properties of the fresh and used Co_{SA}-CNF.

Sample	S_{BET} (m^2/g)	$S_{external}$ (m^2/g)	$V_{micropore}$ (cm^3/g)	$V_{mesopore}$ (cm^3/g)
Co_{SA}-CNF	709	157	0.29	0.54
Co_{SA}-CNF-SDZ	82	73	0.004	0.33
Co_{SA}-CNF-ROX	163	142	0.019	0.48

References

[S1] X. Zhou, X. Zhou, THE UNIT PROBLEM IN THE THERMODYNAMIC CALCULATION OF ADSORPTION USING THE LANGMUIR EQUATION, Chemical Engineering Communications, 201 (2014) 1459-1467.

[S2] J.C. Serna-Carrizales, V.H. Collins-Martínez, E. Flórez, C.F.A. Gomez-Duran, G. Palestino, R. Ocampo-Pérez, Adsorption of sulfamethoxazole, sulfadiazine and sulfametazine in single and ternary systems on activated carbon. Experimental and DFT computations, Journal of Molecular Liquids, 324 (2021) 114740.

[S3] X. Geng, S. Lv, J. Yang, S. Cui, Z. Zhao, Carboxyl-functionalized biochar derived from walnut shells with enhanced aqueous adsorption of sulfonamide antibiotics, Journal of Environmental Management, 280 (2021) 111749.

[S4] M. Wang, X.-y. You, Efficient adsorption of antibiotics and heavy metals from aqueous solution by structural designed PSSMA-functionalized-chitosan magnetic composite, Chemical Engineering Journal, 454 (2023) 140417.

[S5] L. Han, P. Qin, M. Li, D. Li, M. Mu, Y. Gao, S. Zhu, M. Lu, Z. Cai, Hierarchically porous zirconium-based metal–organic frameworks for rapid adsorption and enrichment of sulfonamide antibiotics, Chemical Engineering Journal, 456 (2023) 140969.

[S6] J. Berges, S. Moles, M.P. Ormad, R. Mosteo, J. Gómez, Antibiotics removal from aquatic environments: adsorption of enrofloxacin, trimethoprim, sulfadiazine, and amoxicillin on vegetal powdered activated carbon, Environmental Science and Pollution Research, 28 (2021) 8442-8452.

[S7] H. Yu, K. Zheng, X. Xu, X. Liu, B. Zhao, H. Ding, Z. Yu, C. Deng, Preparation of β-cyclodextrin/dopamine hydrochloride-graphene oxide and its adsorption properties for sulfonamide antibiotics, Environmental Science and Pollution Research, 29 (2022) 70192-70201.

[S8] X.-Y. Zeng, Y. Wang, R.-X. Li, H.-L. Cao, Y.-F. Li, J. Lü, Impacts of temperatures and phosphoric-acid modification to the physicochemical properties of biochar for excellent sulfadiazine adsorption, Biochar, 4 (2022) 14.

[S9] Y. Liu, Y. Peng, B. An, L. Li, Y. Liu, Effect of molecular structure on the adsorption affinity of sulfonamides onto CNTs: Batch experiments and DFT calculations, Chemosphere, 246 (2020) 125778.

[S10] J. Hu, Z. Tong, Z. Hu, G. Chen, T. Chen, Adsorption of roxarsone from aqueous solution

by multi-walled carbon nanotubes, Journal of Colloid and Interface Science, 377 (2012) 355-361.

[S11] W. Fan, X. Zhang, Y. Zhang, P. Wang, L. Zhang, Z. Yin, J. Yao, W.J.J.o.M.R. Xiang, Functional organic material for roxarsone and its derivatives recognition via molecular imprinting, 31 (2018) e2625.

[S12] X. Yu, X. Han, C. Chang, Y. Hu, C. Xu, S. Fang, Corncob-derived activated carbon for roxarsone removal from aqueous solution: isotherms, kinetics, and mechanism, Environmental Science and Pollution Research, 27 (2020) 15785-15797.

[S13] Z. Wen, R. Chen, G. Zhang, S. Li, Y. Zhang, X. Liao, G. Cheng, R. Chen, Selective adsorption and special recognition of roxarsone (ROX) from water by utilizing novel core-shell magnetic molecularly imprinted polymers, Journal of Cleaner Production, 423 (2023) 138801.

[S14] D. Kong, L.D. Wilson, Synthesis and characterization of cellulose-goethite composites and their adsorption properties with roxarsone, Carbohydrate Polymers, 169 (2017) 282-294.